Nucleon polarization in exclusive deuteron electrodisintegration with polarized electrons and a polarized target

Hartmuth Arenhövel,[1] Winfried Leidemann,[2] and Edward L. Tomusiak[3]
[1]*Institut für Kernphysik, Johannes Gutenberg-Universität, D-55099 Mainz, Germany*
[2]*Dipartimento di Fisica, Università di Trento, I-38050 Povo, Italy*
[3]*Department of Physics and Engineering Physics and Saskatchewan Accelerator Laboratory, University of Saskatchewan, Saskatoon, Canada S7N 0W0*
(Received 3 May 1995)

Nucleon polarization in exclusive electrodisintegration of the deuteron using a polarized beam and an oriented target is systematically investigated in a nonrelativistic framework but with lowest order relativistic contributions to the one-body current including the kinematic part of the wave function boost. The structure functions and the asymmetries corresponding to the various nucleon polarization components are studied with respect to their sensitivity to the potential model, to subnuclear degrees of freedom, and to relativistic effects in different kinematical regions. Furthermore, a few new observables are found which are very sensitive to the neutron electric form factor G_{En} in the quasifree region.

PACS number(s): 21.45.+v, 13.40.Gp, 24.70.+s, 25.30.Fj

I. INTRODUCTION

Some years ago we started a systematic study of deuteron electrodisintegration with special emphasis on polarization observables [1–3]. As stated previously, the main purpose of this study is to reveal to what extent the use of polarized electrons and polarized targets and polarization analysis of the outgoing nucleons will allow a considerably more detailed investigation of the dynamical features of the two-nucleon system than is possible without the use of polarization. Specifically, our interest is focused on the role of the NN interaction model, of subnuclear degrees of freedom (DOF) in terms of meson and isobar DOF, and, as a new subject in the present paper, the role of relativistic effects. In view of current interest in the electric form factor of the neutron G_{En}, we will also study the sensitivity of the polarization observables to G_{En}.

In the first paper of this investigation [1] we considered the inclusive process and then in [2] the exclusive one $\vec{d}(\vec{e},e'N)N$ including beam and target polarization but without analysis of the outgoing nucleon polarization. Most recently, as an extension to previous work in photodisintegration [4,5] we have formally derived in [3] all possible polarization structure functions, in total 648, and linear relations between them since only 324 can be linearly independent, considering the fact that each structure function is a Hermitian form of 18 independent complex t-matrix elements. Formal expressions for polarization observables using a different representation scheme for the structure functions have also been given in Ref. [6]. Considering besides electron polarization and deuteron orientation only the polarization of one of the outgoing nucleons, the authors of Ref. [6] find altogether 162 independent structure functions. This is exactly the same number which we find in [3] if we restrict the observables to differential cross section and polarization components of only one final nucleon. However, this set is not complete in the sense that there exists an additional set of 162 structure functions which are linearly independent from the previous ones. As we have outlined in [3] (see Table 6) a possible complete set of linearly independent structure functions comprises, e.g., the differential cross section, the polarization components of one nucleon, $P_y(p)$, $P_{x/z}(p)$, $P_{x/z}(n)$, and the polarization correlations of both nucleons, P_{xx} and P_{xz}.

With the present work we want to conclude this study by looking at the polarization of one or both of the final state nucleons in the exclusive processes $d(e,e'N)N$ and $d(e,e'NN)$ with various combinations of beam and target polarizations. Polarization of one outgoing nucleon in this reaction has been studied previously in [7–13], mainly in the quasifree region for investigation of the electric form factor of the neutron [8,9], relativistic [12,13], or other specific effects [10,11]. In [13] the influence of an oriented deuteron target has been considered in order to study subnuclear DOF and relativistic effects but only for one quasifree kinematics. However, no systematic study exists of how the various dynamic ingredients mentioned above manifest themselves in one- and two-nucleon polarization observables including beam and target polarization with respect to different kinematic regions of energy and momentum transfers. This is the principal goal of the present work.

First we will briefly review in Sec. II the definition and the general expressions of the various polarization observables in terms of structure functions and the corresponding polarization asymmetries. The latter constitute the experimental quantities to be determined in an experiment. Then we will present and discuss in Sec. III the results of our explicit evaluation of the structure functions and asymmetries for the same kinematic regions chosen in [2] in order to represent different areas of sensitivities to final state interactions (FSI's), to subnuclear DOF in wave functions and interaction currents, and relativistic contributions. The calculational framework is essentially the same nonrelativistic one with inclusion of meson exchange currents (MEC's) and iso-

bar configurations or currents (IC's) as described in [1] except for the relativistic contributions to one-body currents as discussed in [12]. With respect to the treatment of IC's in [13] ours is much superior since we do not use the static approximation as in [13], thus allowing us to consider kinematic regions away from the quasifree ridge and excitations up to the Δ region. Furthermore, we also include the most important kinematic part of the wave function boost for the relativistic contributions.

II. OBSERVABLES AND ASYMMETRIES

We start from Eq. (58) of [3] for a general observable X in exclusive deuteron electrodisintegration:

$$\mathscr{O}(X)=P(X)S_0=c\sum_{I=0}^{2}P_I^d\sum_{M=0}^{I}\left\{[\rho_L f_L^{IM}(X)+\rho_T f_T^{IM}(X)+\rho_{LT}f_{LT}^{IM+}(X)\cos\phi+\rho_{TT}f_{TT}^{IM+}(X)\cos 2\phi]\cos\left(M\tilde{\phi}-\bar{\delta}_I^X\frac{\pi}{2}\right)\right.$$
$$-[\rho_{LT}f_{LT}^{IM-}(X)\sin\phi+\rho_{TT}f_{TT}^{IM-}(X)\sin 2\phi]\sin\left(M\tilde{\phi}-\bar{\delta}_I^X\frac{\pi}{2}\right)+h\left[[\rho_T' f_T'^{\,IM}(X)+\rho_{LT}' f_{LT}'^{\,IM-}(X)\cos\phi]\right.$$
$$\left.\left.\times\sin\left(M\tilde{\phi}-\bar{\delta}_I^X\frac{\pi}{2}\right)+\rho_{LT}' f_{LT}'^{\,IM+}(X)\sin\phi\cos\left(M\tilde{\phi}-\bar{\delta}_I^X\frac{\pi}{2}\right)\right]\right\}d_{M0}^I(\theta_d)\ , \tag{1}$$

with

$$c=\frac{\alpha}{6\pi^2}\frac{k_2^{\rm lab}}{k_1^{\rm lab}q_\nu^4}\ . \tag{2}$$

Here α is the fine structure constant and $k_1^{\rm lab}$ and $k_2^{\rm lab}$ denote the laboratory frame momenta of the initial and the scattered electrons, respectively, while $q_\nu^2=q_0^2-\vec{q}^{\,2}$ is the four-momentum transfer squared ($q=k_1-k_2$). The virtual photon density matrix is given by

$$\rho_L=-\beta^2q_\nu^2\frac{\xi^2}{2\eta}\ ,\quad \rho_{LT}=-\beta q_\nu^2\frac{\xi}{\eta}\sqrt{\frac{\xi+\eta}{8}}\ , \tag{3}$$

$$\rho_T=-\frac{1}{2}q_\nu^2\left(1+\frac{\xi}{2\eta}\right)\ ,\quad \rho_{TT}=q_\nu^2\frac{\xi}{4\eta}\ , \tag{4}$$

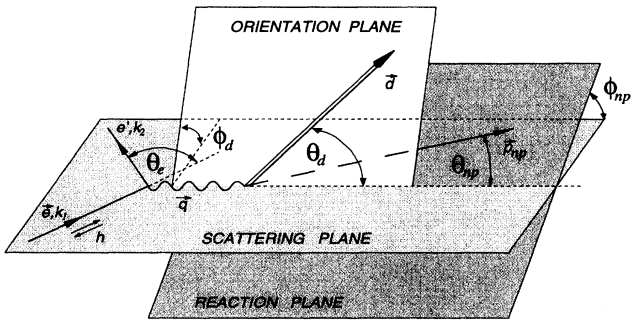

FIG. 1. Geometry of exclusive electron-deuteron scattering with polarized electrons and an oriented deuteron target. The relative n-p momentum defining with $\vec{q}$ the reaction plane is denoted by $\vec{p}_{np}$ and is characterized by angles $\theta=\theta_{np}$ and $\phi=\phi_{np}$. The deuteron orientation axis forming with $\vec{q}$ the orientation plane is denoted by $\vec{d}$ and specified by angles θ_d and ϕ_d.

$$\rho_{LT}'=-\frac{1}{2}\beta q_\nu^2\frac{\xi}{\sqrt{2\eta}}\ ,\quad \rho_T'=-\frac{1}{2}q_\nu^2\sqrt{\frac{\xi+\eta}{\eta}}\ , \tag{5}$$

with

$$\beta=\frac{|\vec{q}^{\,\rm lab}|}{|\vec{q}^{\,c}|}\ ,\quad \xi=-\frac{q_\nu^2}{(\vec{q}^{\,\rm lab})^2}\ ,\quad \eta=\tan^2\left(\frac{\theta_e^{\rm lab}}{2}\right)\ , \tag{6}$$

where $\theta_e^{\rm lab}$ denotes the electron scattering angle in the laboratory system and β expresses the boost from the laboratory system to the frame in which the hadronic tensor is evaluated and $\vec{q}^{\,c}$ denotes the momentum transfer in this frame. Often the hadronic tensor and thus the observables are calculated in the final n-p c.m. system. This system, which sometimes is also called antilaboratory system, moves in the laboratory with total momentum $\vec{q}^{\,\rm lab}$. In this case one has $\vec{q}^{\,c}=\vec{q}^{\,\rm c.m.}$.

Furthermore, $S_0=d^3\sigma_0/dk_2^{\rm lab}d\Omega_e^{\rm lab}d\Omega_{np}^{\rm c.m.}$ denotes the unpolarized differential cross section. For the deuteron density matrix we have assumed a diagonal form with respect to an axis $\hat{d}$ which is called the orientation axis. Therefore, the deuteron target is characterized by four parameters, namely, the vector and tensor polarizations P_1^d and P_2^d, respectively, and by the angles θ_d and ϕ_d describing the direction of the orientation axis $\hat{d}$ of the polarized deuteron target with respect to the coordinate system associated with the scattering plane (see Fig. 1). Note that the deuteron density matrix undergoes no change in the transformation from the laboratory to the c.m. system, since the boost to the c.m. system is collinear with the deuteron quantization axis [14].

TABLE I. Notation for the Cartesian components of the spin observables and their division into sets A and B.

Observable	1	$x0$	$y0$	$z0$	$0x$	$0y$	$0z$		
Set	A	B	A	B	B	A	B		
Observable	xx	xy	xz	yx	yy	yz	zx	zy	zz
Set	A	B	A	B	A	B	A	B	A

The final two-nucleon state in the c.m. frame is described by the relative momentum $\vec{p}_{np}$ characterized by the angles θ and ϕ. The angle $\tilde{\phi}=\phi-\phi_d$ is the angle between the orientation and the reaction planes, while ϕ is the angle between the reaction and the scattering planes (see Fig. 1). The longitudinal electron polarization is denoted by h. The various observables X are listed in Table I. The components of the polarization components of both particles refer to the reference frame associated with the final n-p c.m. system denoted by (x, y, z). It is the same as $(\bar{x}, \bar{y}, \bar{z})$ in [4]. Its z axis is parallel to $\vec{p}_{np}$ in the reaction plane and its y axis parallel to $\vec{q}\times\vec{p}_{np}$ perpendicular to the reaction plane. Thus the polarization components of particle 1 (here the proton) are chosen according to the Madison convention while for particle 2 (neutron) the x and z components of $\vec{P}$ have to be reversed in order to comply with this convention. This is done for the presentation of our results on structure functions and polarization asymmetries. The observables, listed in Table I, are divided into two sets called A and B according to their behavior under a parity transformation [5]. Furthermore, we have introduced in (1)

$$\bar{\delta}_I^X=(\delta_{X,B}-\delta_{I1})^2 , \tag{7}$$

where

$$\delta_{X,B}:=\begin{cases}1 & \text{for } X\in B,\\ 0 & \text{for } X\in A.\end{cases} \tag{8}$$

For later purposes we define $\delta_{X,A}:=1-\delta_{X,B}$. Finally the structure functions[1] $f_\alpha^{(\prime)\,IM(\pm)}(X)$ ($\alpha=L, T, LT, TT$) contain the complete information on the dynamical properties of the NN system available in deuteron electrodisintegration. They are functions of θ, E_{np}, and $\vec{q}_{\text{c.m.}}^{\,2}$, the relative n-p energy, and the three-momentum transfer squared, respectively, both in the c.m. system. Explicit expressions can be found in [3] and are listed for convenience in Appendix A. We would like to remark that compared to the definition of the structure functions in [2] we have incorporated in [3] in the definition of $f'^{\,IM(\pm)}_\alpha(X)$ the phase factor $(-)^I$ which appears explicitly in Eq. (27) of [2] in that part which depends on the longitudinal electron polarization.

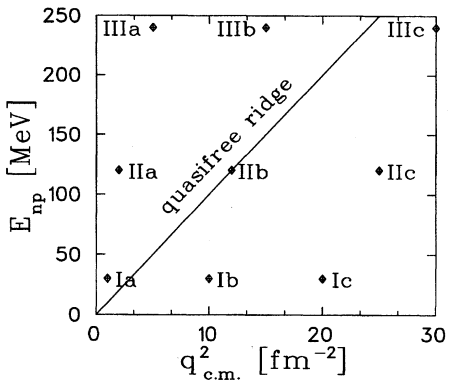

FIG. 2. E_{np}- $\vec{q}^{\,2}_{\text{c.m.}}$ plane with indication of the location of the quasifree ridge and the kinematic sectors, for which the structure functions have been evaluated.

In analogy to the asymmetries introduced in [2] for the differential cross section we now define corresponding quantities for each observable X by

$$P(X)=P_0(X)+P_1^dP_d^V(X)+P_2^dP_d^T(X)+h[P_e(X)+P_1^dP_{ed}^V(X)+P_2^dP_{ed}^T(X)] , \tag{9}$$

which we will call in general polarization asymmetries even for $P_0(X)$. By comparison with (1) one finds explicitly

$$P_0(X)=\frac{c}{S_0}[(\rho_Lf_L^{00}(X)+\rho_Tf_T^{00}(X)+\rho_{LT}f_{LT}^{00+}(X)\cos\phi+\rho_{TT}f_{TT}^{00+}(X)\cos2\phi]\delta_{X,A} ,$$
$$+[\rho_{LT}f_{LT}^{00-}(X)\sin\phi+\rho_{TT}f_{TT}^{00-}(X)\sin2\phi]\delta_{X,B}] , \tag{10}$$

$$P_d^V(X)=\frac{c}{S_0}\sum_{M=0}^{1}\left[(\rho_Lf_L^{1M}(X)+\rho_Tf_T^{1M}(X)+\rho_{LT}f_{LT}^{1M+}(X)\cos\phi+\rho_{TT}f_{TT}^{1M+}(X)\cos2\phi)\cos\left(M\tilde{\phi}-\delta_{X,A}\frac{\pi}{2}\right)\right.$$
$$\left.-[\rho_{LT}f_{LT}^{1M-}(X)\sin\phi+\rho_{TT}f_{TT}^{1M-}(X)\sin2\phi]\sin\left(M\tilde{\phi}-\delta_{X,A}\frac{\pi}{2}\right)\right]d^1_{M0}(\theta_d) , \tag{11}$$

$$P_d^T(X)=\frac{c}{S_0}\sum_{M=0}^{2}\left[[\rho_Lf_L^{2M}(X)+\rho_Tf_T^{2M}(X)+\rho_{LT}f_{LT}^{2M+}(X)\cos\phi+\rho_{TT}f_{TT}^{2M+}(X)\cos2\phi]\cos\left(M\tilde{\phi}-\delta_{X,B}\frac{\pi}{2}\right)\right.$$
$$\left.-[\rho_{LT}f_{LT}^{2M-}(X)\sin\phi+\rho_{TT}f_{TT}^{2M-}(X)\sin2\phi]\sin\left(M\tilde{\phi}-\delta_{X,B}\frac{\pi}{2}\right)\right]d^2_{M0}(\theta_d) , \tag{12}$$

[1]Primed and unprimed structure functions are here referred to collectively as $f_\alpha^{(\prime)\,IM(\pm)}(X)$.

$$P_e(X)=\frac{c}{S_0}\{-[\rho'_T f'^{\,00}_T(X)+\rho'_{LT} f'^{\,00-}_{LT}(X)\cos\phi]\delta_{X,B}+\rho'_{LT} f'^{\,00+}_{LT}(X)\sin\phi\ \delta_{X,A}\}\ , \tag{13}$$

$$P^V_{ed}(X)=\frac{c}{S_0}\sum_{M=0}^{1}\left[[\rho'_T f'^{\,1M}_T(X)+\rho'_{LT} f'^{\,1M-}_{LT}(X)\cos\phi]\sin\left(M\tilde{\phi}-\delta_{X,A}\frac{\pi}{2}\right)+\rho'_{LT} f'^{\,1M+}_{LT}(X)\sin\phi\cos\left(M\tilde{\phi}-\delta_{X,A}\frac{\pi}{2}\right)\right]d^1_{M0}(\theta_d)\ , \tag{14}$$

$$P^T_{ed}(X)=\frac{c}{S_0}\sum_{M=0}^{2}\left[[\rho'_T f'^{\,2M}_T(X)+\rho'_{LT} f'^{\,2M-}_{LT}(X)\cos\phi]\sin\left(M\tilde{\phi}-\delta_{X,B}\frac{\pi}{2}\right)+\rho'_{LT} f'^{\,2M+}_{LT}(X)\sin\phi\cos\left(M\tilde{\phi}-\delta_{X,B}\frac{\pi}{2}\right)\right]d^2_{M0}(\theta_d)\ . \tag{15}$$

For the differential cross section ($X=1$) we remind the reader that one has with respect to the notation in [2,9]

$$P_0(1)=1,\quad P^{V/T}_d=A^{V/T}_d,\quad P_e(1)=A_e,\quad P^{V/T}_{e,d}=A^{V/T}_{e,d}\ . \tag{16}$$

In [2] we have described in detail how the asymmetries can be separated experimentally by proper choice of the polarization parameters h, P^d_1, and P^d_2. The further separation of the polarization structure functions $f^{(\prime)\,IM(\pm)}_\alpha(X)$ by exploiting the dependence of the asymmetries on ϕ, ϕ_d, and θ_d has also been discussed in detail in [2] for an observable of type A, because the method applied in [2] to the differential cross section works in general for an arbitrary observable $X\in A$. An analogous procedure can be used for an observable $X\in B$. Since we have found in the meantime a few more optimal settings compared to [2], we summarize in Appendix B the settings for both types of observables. One should be aware that for an observable $X\neq 1$ the quantity P_X is usually defined with respect to the corresponding differential cross section including the beam and target polarization, i.e.,

$$P_X(h,P^d_1,P^d_2)=P(X)/P(1)=P(X)/[1+P^d_1A^V_d+P^d_2A^T_d+h(A_e+P^d_1A^V_{ed}+P^d_2A^T_{ed})]\ , \tag{17}$$

where $P(X)$ is given in (9). This completes the brief formal part, and now we can turn to the presentation and discussion of our results.

III. RESULTS AND DISCUSSION

As already mentioned in the Introduction, the various structure functions $f^{(\prime)\,IM(\pm)}_\alpha$ are calculated within the same nonrelativistic framework that has been used previously in [1,2]. It is described in detail in Ref. [7] with the one exception that we do not use the nonrelativistic approximation in the kinematical factors of the T matrix but take instead the relativistic expressions as given in Eq. (61) of Ref. [9]. In addition we include the most important relativistic contributions to the one-body current, which are those arising from the nonrelativistic reduction of the Dirac current and the kinematic boost as described in [12]. In the calculation of the t-matrix elements we calculate explicitly all electric and magnetic multipoles up to the order $L=6$. That means we include the final state interaction in all partial waves up to $j=7$. For the higher multipoles we use the Born approximation for the final state, i.e., no final state interaction in partial waves with $j\geq 8$ as has been described in Ref. [7]. We would like to remark that for the electric transitions we use the Siegert operators in the convention of [15] except in the case of the Born approximation. In this way the major MEC contribution is incorporated implicitly.

For the calculation of the initial deuteron and the final n-p scattering wave functions we use the Nijmegen [16], the Paris [17], Bonn [18] (r-space version), and Argonne V_{14} and V_{28} potentials [19]. The latter explicitly includes Δ degrees of freedom within a coupled channel (CC) approach. Above the pion threshold V_{28} is modified for the $^1D_2$ partial wave in order to give a better description of this channel as described in Ref. [20]. For the other potential models we use the impulse approximation for the calculation of the IC's [21,22]. In the current operator we include explicit meson exchange contributions beyond the Siegert operators, essentially from π and ρ exchange, and isobar contributions. For the electromagnetic form factors of the one-body current we use the dipole fit with a nonvanishing neutron electric form factor [23]. The electromagnetic nucleon form factors are taken in the Sachs form which has the advantage that the next to leading order relativistic contributions to the charge density are considerably reduced [12]. For this reason we expect in general relativistic effects to be significantly smaller than reported in [13] where Dirac-Pauli form factors are considered. Finally, for the MEC form factor we use G^V_E. The structure functions are calculated in the c.m. system of the final n-p state. In detail we will investigate the following effects: The influence of FSI MEC's beyond the Siegert current and IC's, the potential model dependence, relativistic contributions (RC's) as mentioned above, and the neutron electric form factor G_{En}.

In addition to their dependence on the relative c.m. n-p angle θ, the structure functions $f^{(\prime)\,IM(\pm)}_\alpha$ are also functions of the relative n-p energy E_{np} and the squared three-momentum transfer $\vec{q}^{\,2}_{\rm c.m.}$, both in the c.m. system. As we have outlined in [2], we have chosen for this exploratory study three different cuts in the E_{np}-$\vec{q}^{\,2}_{\rm c.m.}$ plane in order to cover regions with different dynamic properties: A cut at a constant low energy $E_{np}=30$ MeV taking momentum transfers of 1, 10, and 20 fm^{-2}, a second one at a constant inter-

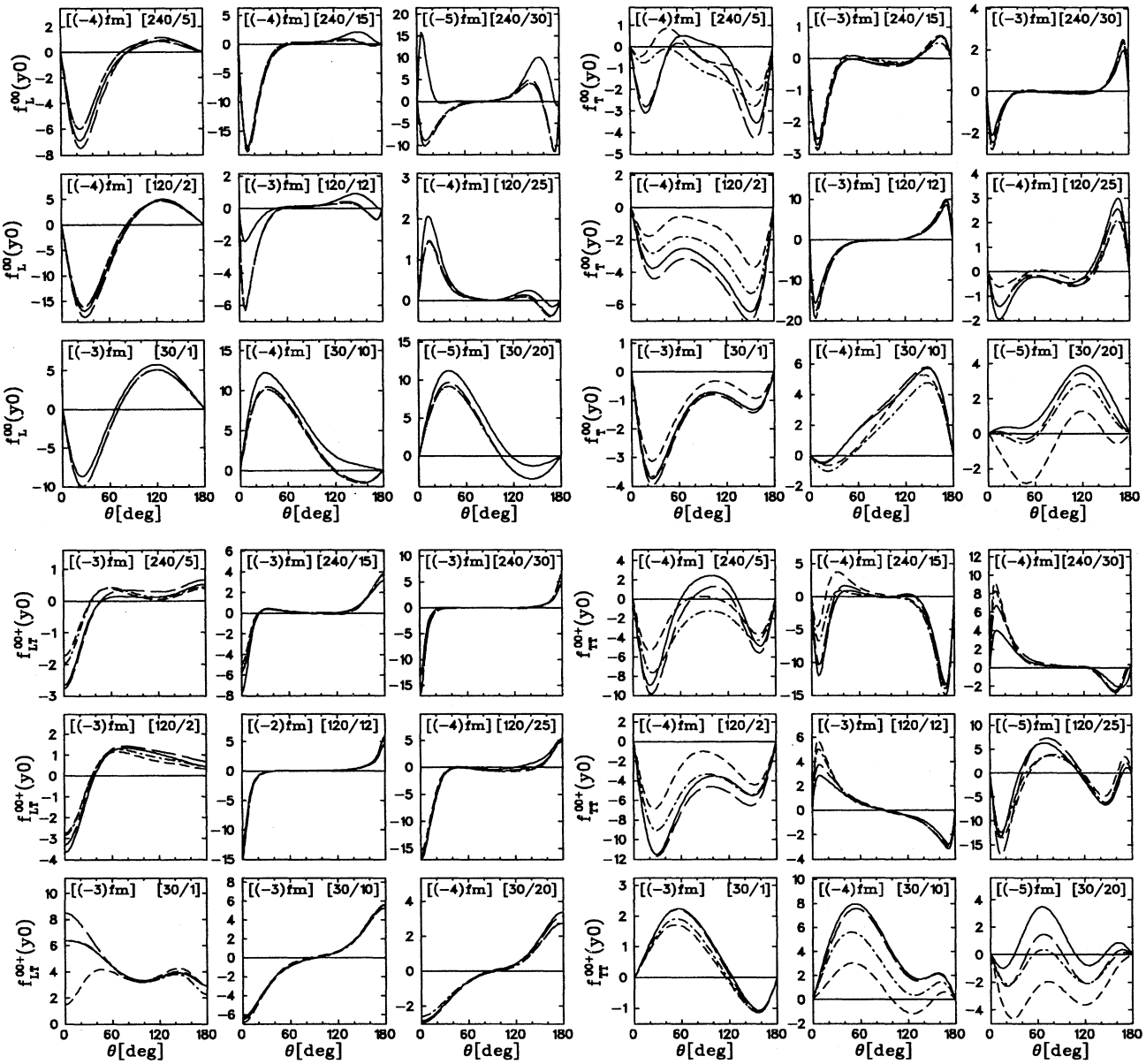

FIG. 3. The structure functions of the observable $P_y(p)$ for unpolarized electrons and target in the nine kinematic regions of Fig. 2: f_L^{00} (top left), f_T^{00} (top right), f_{LT}^{00+} (bottom left), and f_{TT}^{00+} (bottom right). Notation of the curves: N (short dashed line), $N+$MEC (dash-dotted line), $N+$MEC+IC (long dashed line), total$=N+$MEC+IC+RC (solid line), and Born approximation with RC's (dotted line). The top left inset "$[(-n)$ fm]" indicates the unit $[10^{-n}$ fm] for the structure function and the top right inset "$[E_{np}/q^2_{\text{c.m.}}]$," where E_{np} in [MeV] and $q^2_{\text{c.m.}}$ in [fm^{-2}], indicates the kinematic sector of Fig. 2.

mediate energy $E_{np}=120$ MeV choosing momentum transfers of 2, 12, and 25 fm^{-2}, and finally a third cut at $E_{np}=240$ MeV, the region of Δ excitation, with momentum transfers of 5, 15, and 30 fm^{-2}. These different kinematic sectors are marked in Fig. 2 where we also introduce a numbering in order to facilitate the following discussion of the results.

In Ref. [3] we defined a complete set of polarization observables. Knowledge of all structure functions for this set completely determines the process $d+e\rightarrow e'+n+p$. Of the nine double polarization observables one need only to consider a smaller number since many are related to single polarization observables. In fact one requires only one of either xx or zz and one of either xz or zx. In order to complete set A one also requires the observables 1 and $y0$. For the set B the observables $x0$, $0x$, $z0$, and $0z$ form a complete set. It is obvious that we cannot show all the 324 linearly independent structure functions. Thus we will begin with an overview for which we restrict ourselves to an unpolarized deuteron target. In this case one is left with 36 structure functions corresponding to the observables 1, $y0$, xx, xz, $x0$, $0x$, $z0$, and $0z$. The A-type observables consist of four unprimed and one primed structure functions for unpolarized and polarized electrons, respectively, whereas the B-type observables con-

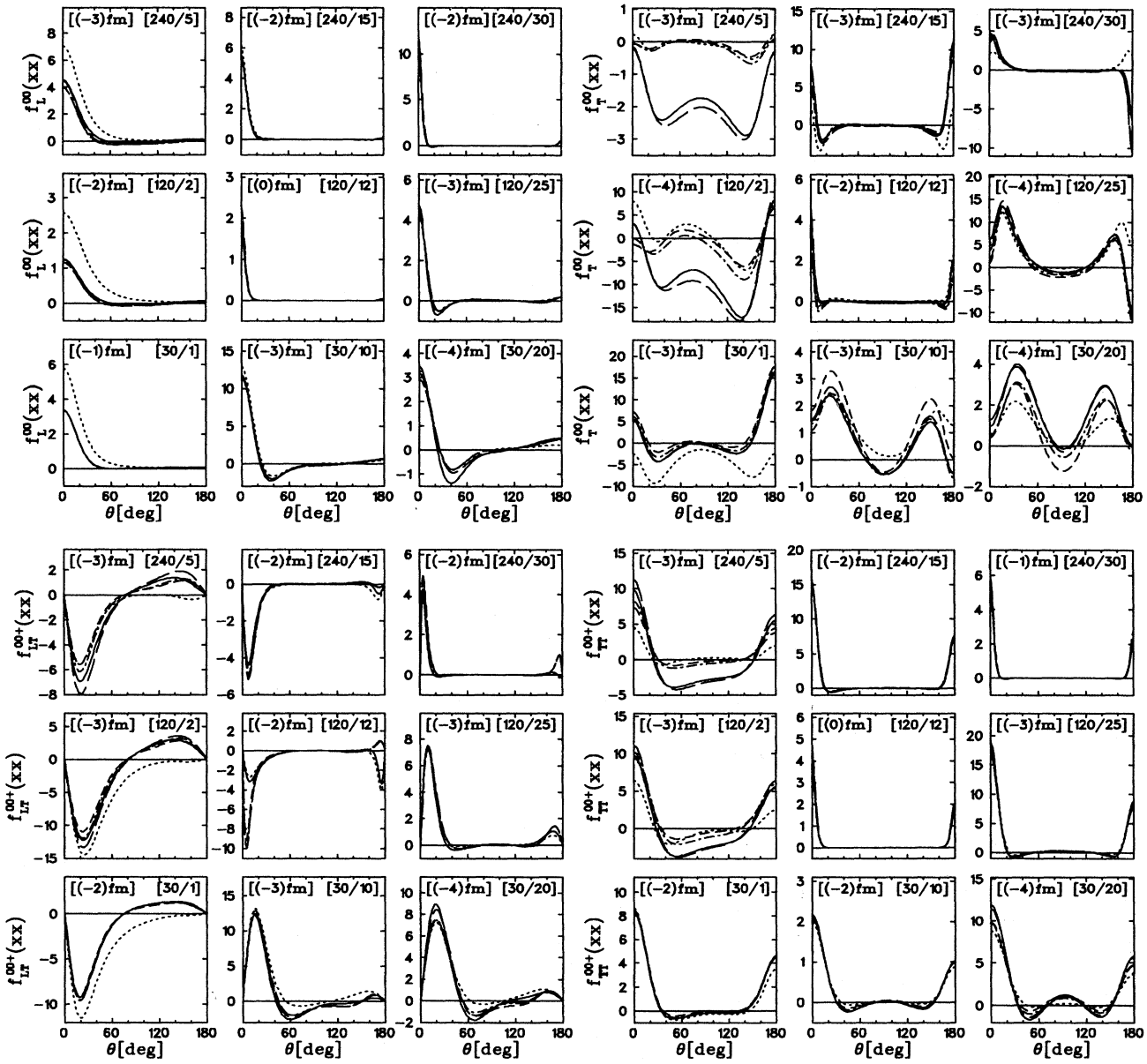

FIG. 4. As Fig. 3 but for the observable P_{xx}.

sist of two unprimed and two primed structure functions [see Eqs. (10) and (13)]. The four unprimed structure functions of observable 1 describe the unpolarized differential cross section and have already been discussed previously in [2]. The remaining 31, calculated with the Paris potential, are illustrated in Figs. 3–10.

Each figure is divided into four (in one case three) panels, each representing one specific structure function. A panel contains in turn nine parts, one for each kinematic sector of Fig. 2 arranged accordingly. In these figures we show separately the so-called normal part (N) without explicit MEC's, IC's, and RC's and then consecutively added explicit MEC's, IC's, and finally RC's. Furthermore, where nonvanishing, the Born approximation including RC's is shown. One should note that the angle θ always refers to the outgoing proton even in the case of neutron polarization structure functions.

Among the structure functions of $P_y(p)$ in Fig. 3 the LT interference one is the largest. It is generally forward peaked and also peaked in the backward direction for higher momentum transfers (sectors Ib/c, IIb/c, and IIIb/c). Except at low momentum transfer, there is little dependence on the various current contributions. These show a stronger influence in the T- and TT-structure functions, in particular away from the quasifree region in the sectors Ib/c, IIa, and IIIa. Relativistic contributions show sizable effects in $f_L^{00}(y0)$ at higher momentum transfers [sectors IIb (quasifree), IIc, and IIIc]. The structure functions of the polarization correlation P_{xx} are shown in Fig. 4. The largest ones are the L- and TT structure functions, especially on the quasifree ridge. Both are strongly forward peaked while the TT function displays also a smaller backward peak. The xx polarization structure functions are particularly interesting at low q: $f_L^{00}(xx)$ and

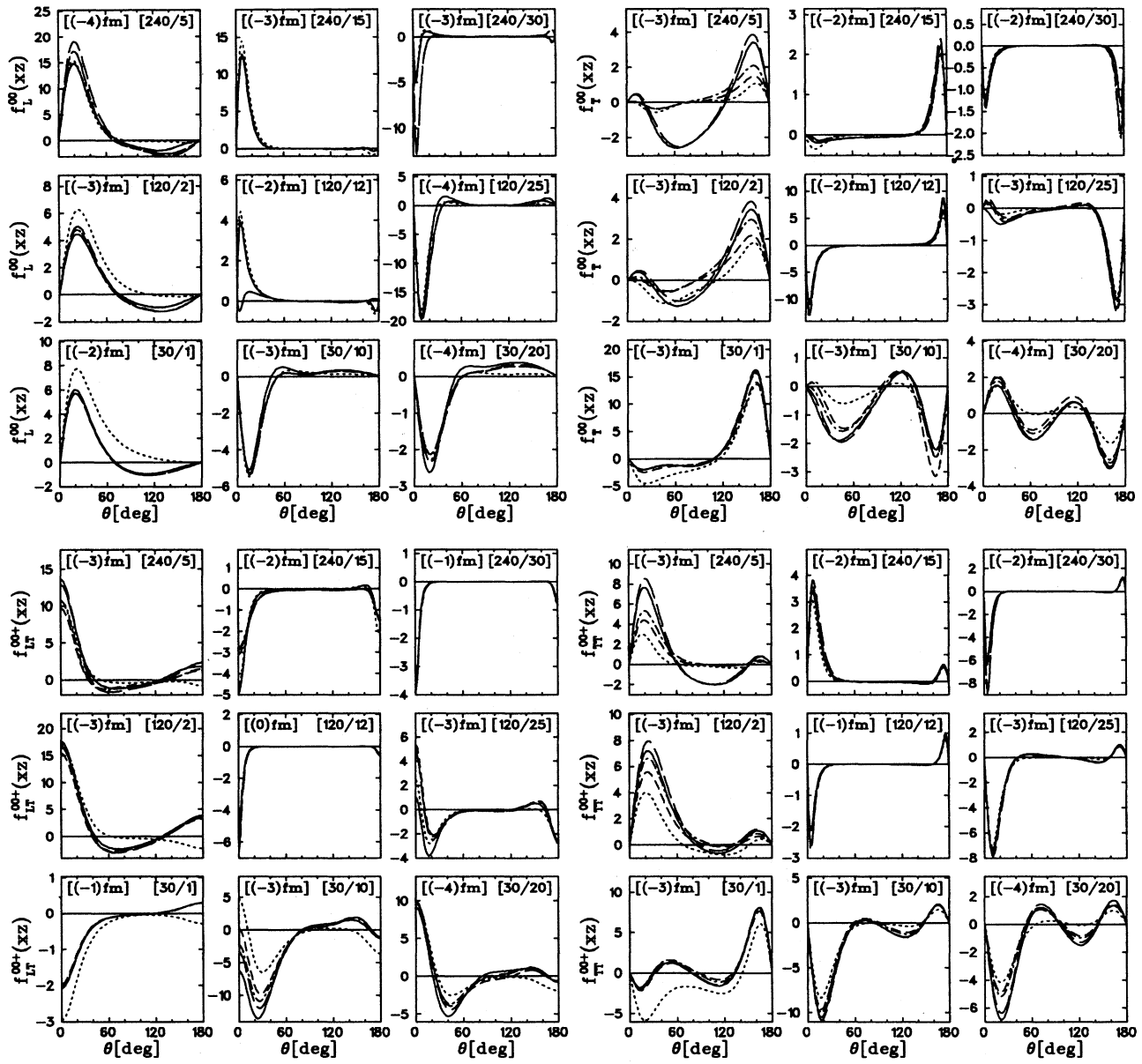

FIG. 5. As Fig. 3 but for the observable P_{xz}.

$f_{LT}^{00+}(xx)$ are sensitive to FSI's (sectors Ia, IIa, and IIIa), while the purely transverse ones—especially $f_T^{00}(xx)$—are sizably influenced by IC's. The other polarization correlation P_{xz} shown in Fig. 5 receives the largest contribution from the LT- and TT-structure functions. Both show a forward peak which is most pronounced at higher q and close to the quasifree kinematics. Remarkably there is a strong RC effect in $f_L^{00}(xz)$ on the quasifree ridge (IIb). Furthermore, one also finds some sensitivity to FSI's and various current contributions at low E_{np} and/or low q (sectors Ia–c, IIa, and IIIa).

For the A-type observables only one primed structure function $f_{LT}'^{00+}(X)$ exists which is the so-called fifth structure function in case of the differential cross section. We show it in Fig. 6 for the observables $y0$, xx, and xz. For $y0$ the only remarkable feature is the pronounced forward peak of $f_{LT}'^{00+}(y0)$, particularly sharp in the sectors IIb, IIIb, and IIIc. One notes some sensitivity to FSI's in sectors Ia and IIa. Quite a different behavior in the various kinematic sectors is seen for xx and xz. Their structure functions are in general an order of magnitude smaller than the ones of $y0$, but show a rather strong sensitivity to MEC's, IC's, and RC's in sector IIIa and in the case of xx also in sector IIc.

Now we will turn to the B-type observables which without beam and target polarization contain only LT- and TT-interference structure functions. They are particularly sensitive to FSI's since they vanish in Born approximation. Figure 7 shows the structure functions for $P_x(p)$ and $P_x(n)$. For both proton and neutron, the dominant one is f_{LT}^{00-}. For the proton it is almost an order of magnitude larger than f_{TT}^{00-}. It is strongly forward and backward peaked in the sectors IIb/c

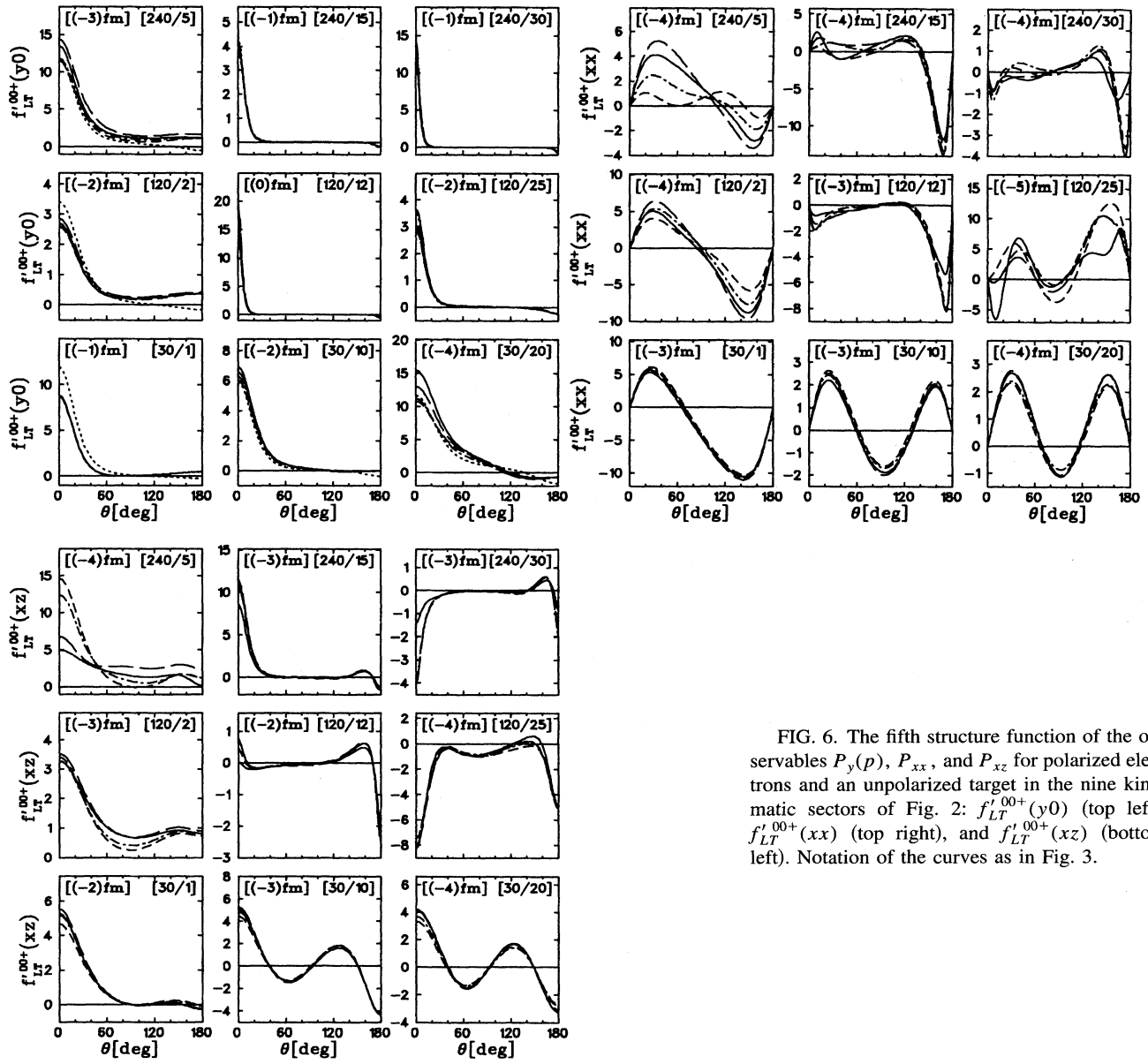

FIG. 6. The fifth structure function of the observables $P_y(p)$, P_{xx}, and P_{xz} for polarized electrons and an unpolarized target in the nine kinematic sectors of Fig. 2: $f'^{00+}_{LT}(y0)$ (top left), $f'^{00+}_{LT}(xx)$ (top right), and $f'^{00+}_{LT}(xz)$ (bottom left). Notation of the curves as in Fig. 3.

and IIIb/c, while in the other sectors it shows a significant size over a larger angular range. In particular in the *a* sectors it exhibits a distinctly different pattern. Here one finds in f^{00-}_{LT} considerable sensitivity to various current contributions, especially strong in the sector Ia for the proton while for the neutron the largest effects are seen in the sectors IIa and IIIa, in particular from IC's and somewhat weaker from RC's. In f^{00-}_{TT} the influence from MEC's and IC's is sizable in all sectors whereas relativistic effects are noticeable in the high-q sectors only. For the other two observables $P_z(p)$ and $P_z(n)$ the LT- and TT-structure functions in Fig. 8 are comparable in magnitude. In contrast to the x components here f^{00-}_{LT} vanishes in the forward and backward directions. Furthermore, f^{00-}_{TT} shows in general a greater sensitivity to subnuclear contributions in the sectors Ia–Ic, IIa, and IIIa. Effects from IC's are particularly strong in sectors IIa and IIIa, while explicit MEC's are especially large for the proton in sectors Ib and Ic.

With respect to the primed structure functions of the B-type observables which require electron polarization, Fig. 9 shows them for $P_x(p)$ and $P_x(n)$. For both proton and neutron, the dominant one is f'^{00-}_{LT} which is strongly forward peaked. For the proton it is almost an order of magnitude larger than f'^{00}_{T}. There is little sensitivity in f'^{00-}_{LT} to FSI's and subnuclear effects while f'^{00}_{T} exhibits some moderate influence at low q or low E_{np}. For the other two observables $P_z(p)$ and $P_z(n)$ the qualitative features of the structure functions in Fig. 10 are almost interchanged. Here f'_T is in general larger than f'^{00-}_{LT}. The latter one for the neutron is strongly modified by FSI's at $E_{np}=30$ MeV and

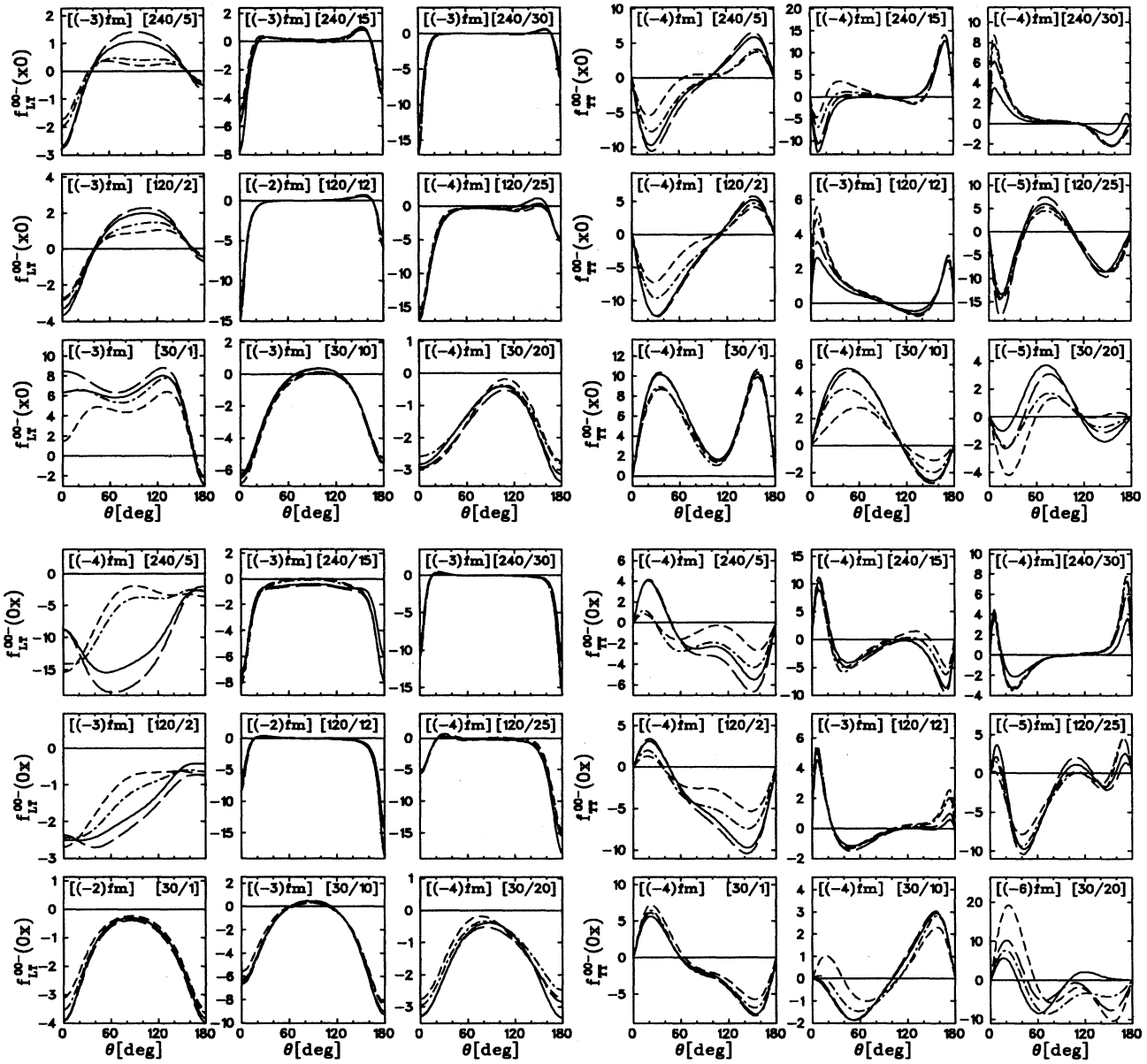

FIG. 7. The structure functions of the observables $P_x(p)$ and $P_x(n)$ for unpolarized electrons and target in the nine kinematic sectors of Fig. 2: $f_{LT}^{00-}(x0)$ (top left), $f_{TT}^{00-}(x0)$ (top right), $f_{LT}^{00-}(0x)$ (bottom left), and $f_{TT}^{00-}(0x)$ (bottom right). Notation of the curves as in Fig. 3.

$\vec{q}^{\,2}_{\text{c.m.}} = 1$ fm^{-2}. Also for the proton one observes sizable FSI effects at low q. This concludes the overview over the structure functions without deuteron orientation.

As mentioned above Figs. 3–10 show only 31 of the 324 independent structure functions and one can easily imagine that a complete experimental determination of deuteron electrodisintegration would be a tremendous experimental effort. However, it is improbable that all of these are sufficiently interesting to warrant a detailed experimental study. For this reason we have scanned all the 324 structure functions with respect to the influence of the theoretical ingredients and made a selection of the most remarkable cases. Therefore, we will present in the following discussion only those structure functions, mostly for an oriented deuteron, which show notable effects due to a specific theoretical ingredient in order to give a guideline for such type of experiments involving an oriented deuteron target.

The most pronounced FSI effects are found in the sector Ia. Figure 11 illustrates two typical examples. Comparing with Fig. 4 one sees that $f_L^{11}(y0)$ and $f_L^{00}(xx)$ are almost identical. The strength of both structure functions is strongly reduced over a large range of angles by FSI's. Furthermore, neither exhibit any dependence on subnuclear DOF or relativistic effects. The second structure function of Fig. 11, $f_{LT}^{11-}(0z)$, shows quite a different and more dramatic behavior. Without FSI's it has a negative forward and a positive backward peak whereas inclusion of FSI's reverses the sign

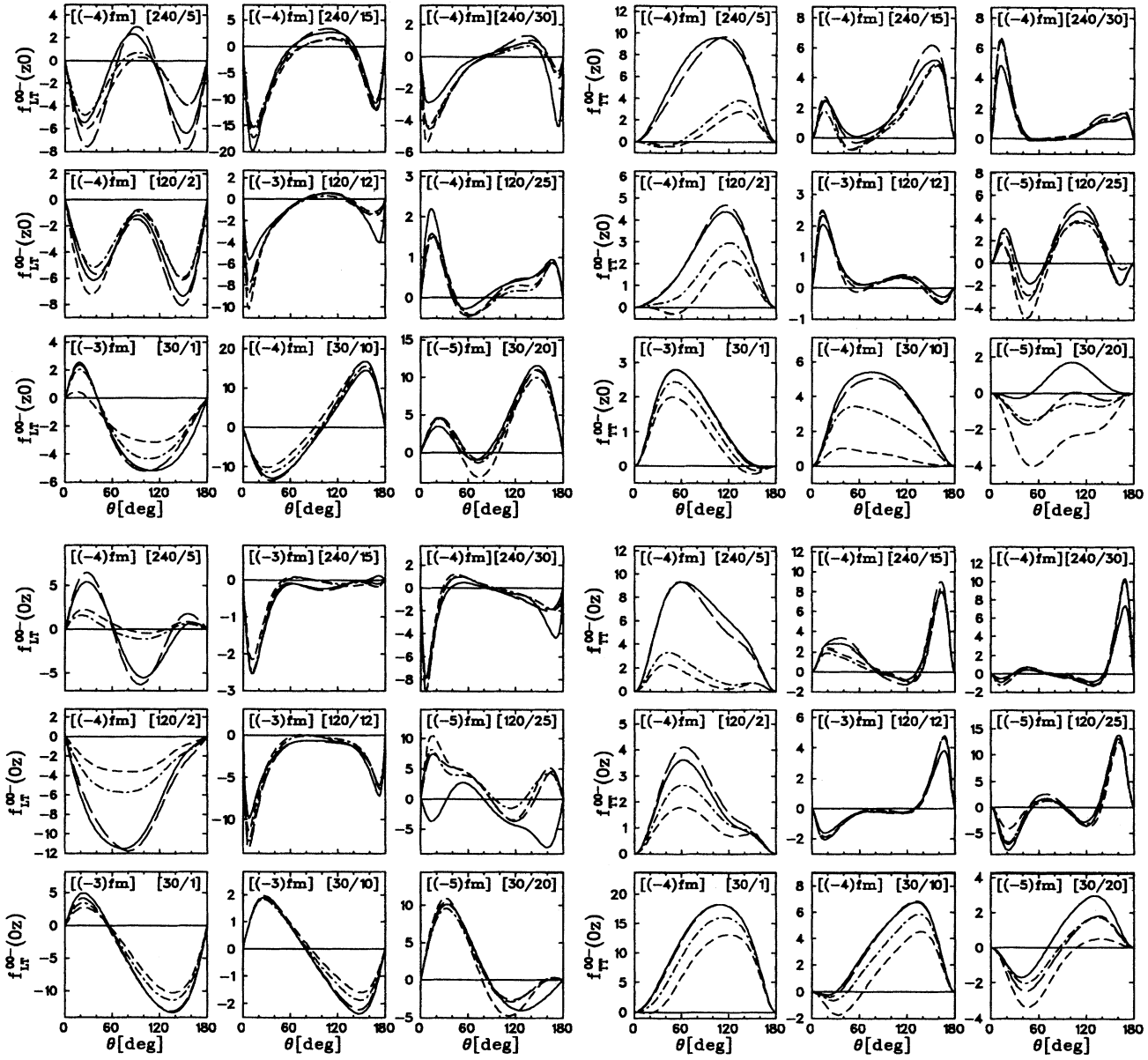

FIG. 8. As Fig. 7 but for the observables $P_z(p)$ and $P_z(n)$. Notation of the curves as in Fig. 3.

of both peaks and, furthermore, increases them in magnitude by almost a factor of 2.

One might expect to find a strong potential model dependence for the above mentioned structure functions, but unfortunately this is not the case. It turns out that all structure functions which show strong FSI effects over a large angular range exhibit almost no potential model dependence. There are of course cases with rather strong potential model effects. However, apart from the above structure functions they vanish without FSI's and sizable potential effects are present only in a smaller angular range. The strongest effects are found in the quasifree region (sector IIb) at forward angles. This is illustrated in Fig. 12, where the structure functions with the strongest dependence on the potential model are shown in the angular range 0°–60°. The most dramatic effect is seen in $f_L^{21}(y0)$ which is positive for the Bonn potential while all other models give a negative value though different in magnitude for Paris and Nijmegen on one side and V_{14} and V_{28} on the other side. This grouping of some potential models is also observed in the other two examples, namely very similar results in $f_{LT}^{00+}(y0)$ for the Bonn and Nijmegen potentials, and V_{14} and V_{28}, respectively. The latter two give also almost equal results for $f_{LT'}^{22+}(0x)$ whereas the other three potential models give each a different prediction. The same structure functions exhibit also relatively large potential model effects in the sector IIc as is illustrated in Fig. 13 for two of them. The relative size of the effect is similar, though somewhat smaller in $f_{LT'}^{22+}(0x)$.

The most remarkable explicit MEC effects are found in the sector Ic for the structure functions $f_{LT'}^{11+}(0x)$ and

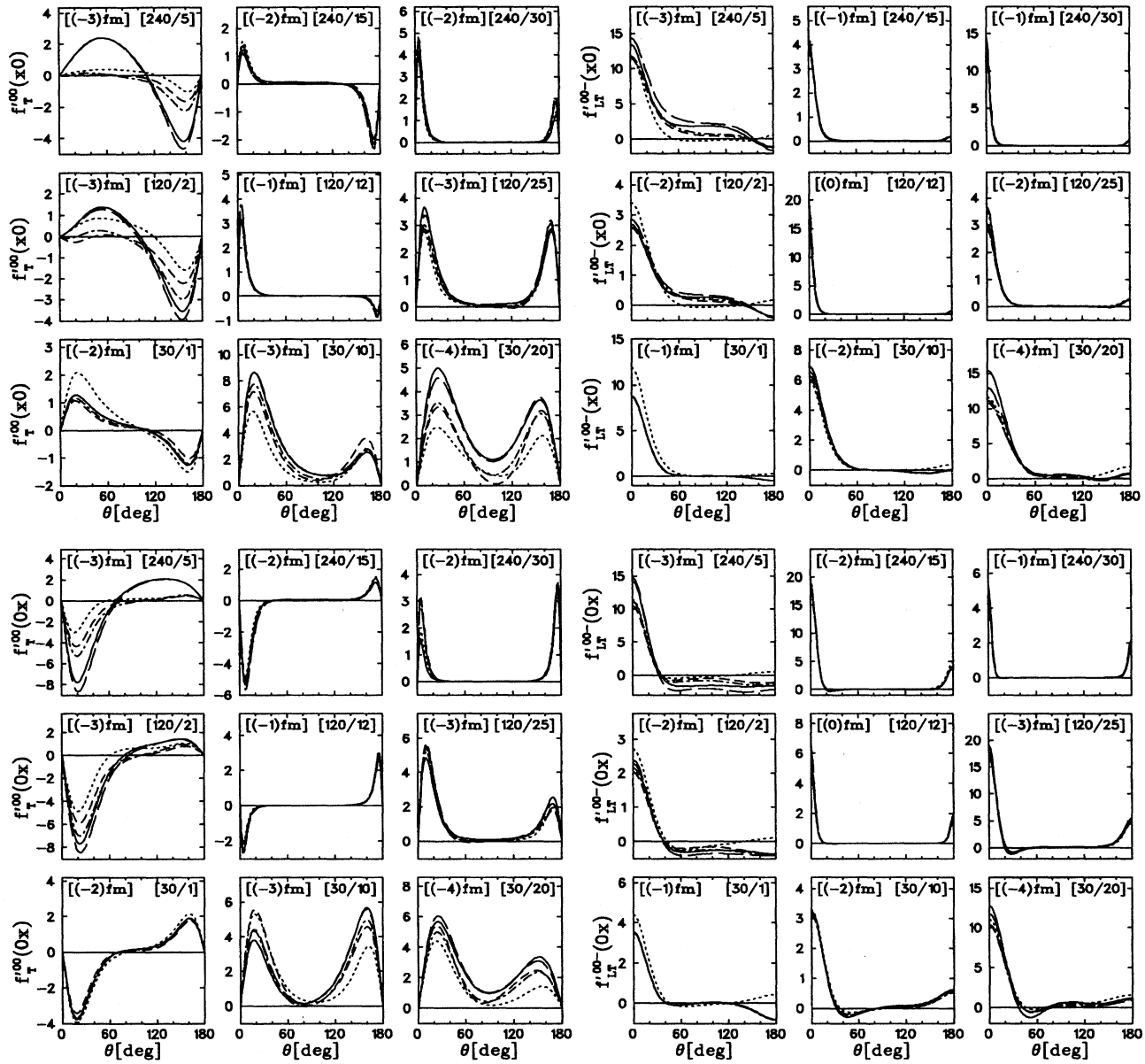

FIG. 9. The structure functions of the observables $P_x(p)$ and $P_x(n)$ for longitudinally polarized electrons but unpolarized target in the nine kinematic sectors of Fig. 2: $f_T'^{00}(x0)$ (top left), $f_{LT}'^{00-}(x0)$ (top right), $f_T'^{00}(0x)$ (bottom left), and $f_{LT}'^{00-}(0x)$ (bottom right). Notation of the curves as in Fig. 3.

$f_{LT}'^{21+}(z0)$. Figure 14 shows that MEC is dominant between 0° and 60°. However, concerning the role of MEC's one should bear in mind that the region near the deuteron breakup threshold offers the best possibilities for their study in $M1$ transitions (see, e.g. [24] and references therein). Here we do not consider this region because polarization experiments cannot lead to significant additional information, since the dominant transverse part is governed by just one transition.

With respect to IC's we discovered a few notable examples. Not surprisingly, the best ones are found in the Δ-resonance region at lower momentum transfer (sector IIIa) and are shown in Fig. 15. All four cases $f_T^{11}(y0)$, $f_T^{10}(z0)$, $f_{TT}^{11-}(0z)$, and $f_{TT}^{22+}(xx)$ exhibit a very strong effect due to IC's, while all other effects remain remarkably small. With Fig. 16 we discuss another aspect of the Δ DOF, namely, the influence of a coupled channel approach with the Argonne V_{28} potential compared to the impulse approximation (IA). We show four particularly interesting cases, where all the four structure functions lead to rather similar results in IA with the four conventional NN potential models, while the results for the V_{28} potential are considerably different. The structure function $f_{LT}'^{00+}(xz)$ is particularly notable, since it exhibits a completely different structure in the CC approach with V_{28}.

Now we turn to the relativistic effects. They are mainly

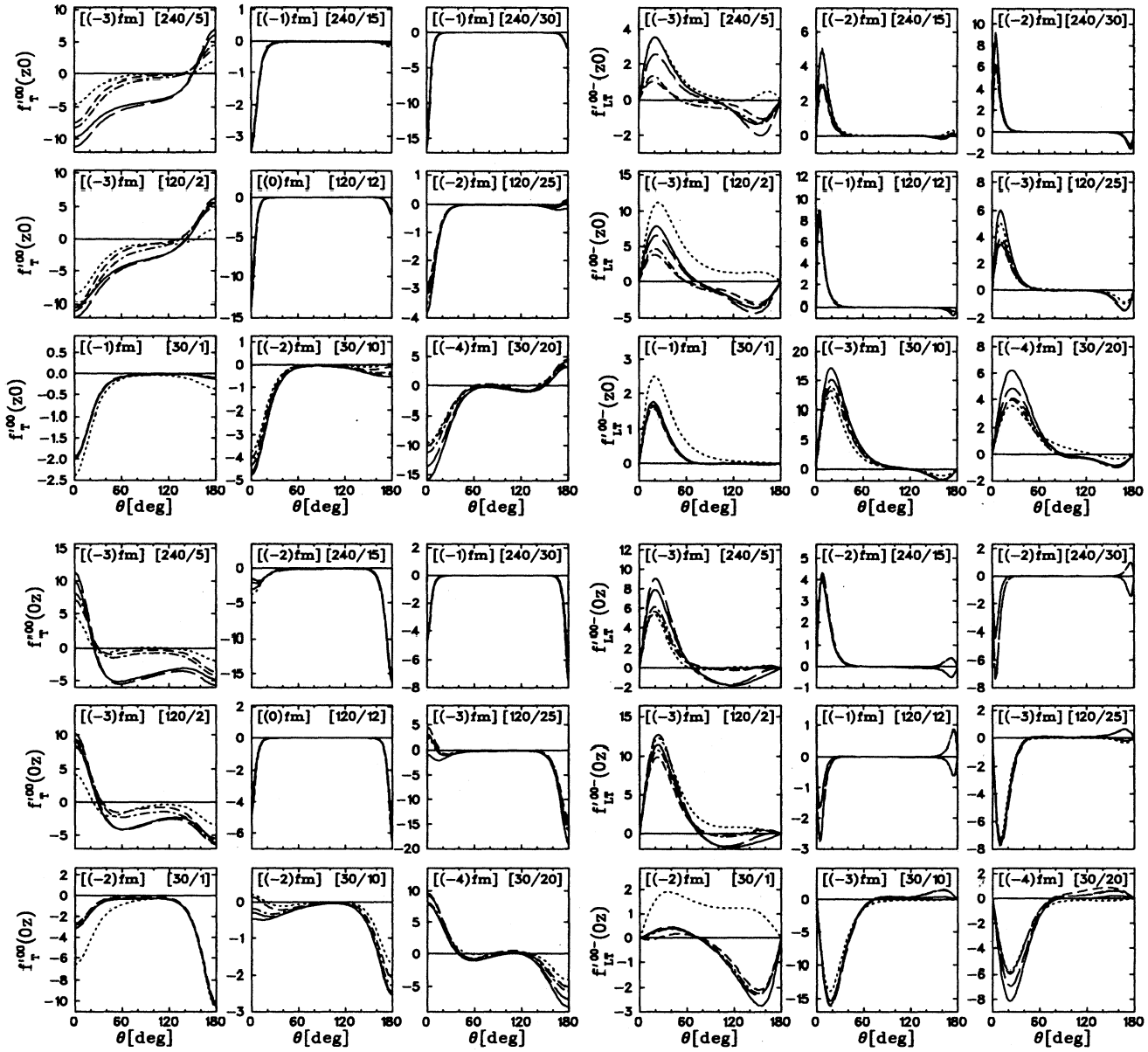

FIG. 10. As Fig. 9 but for the observables $P_z(p)$ and $P_z(n)$. Notation of the curves as in Fig. 3.

present for the LT interference structure functions at higher momentum transfer. Figure 17 shows that $f_{LT}^{11-}(y0)$ is strongly affected at forward angles, whereas $f_{LT}^{10+}(z0)$ is considerably influenced at forward and backward angles, in particular for the higher momentum transfer.

Having discussed the various aspects of FSI's, subnuclear DOF and relativistic contributions, there remains the question of how strongly these effects will show up in the polarization asymmetries. In fact, the signature of any one of these effects could be masked in two ways. First of all, the cross section S_0 in the denominator could be strongly affected by at least one of the theoretical ingredients which could result in a drastic change of the asymmetry. Second, the structure function in question could be too small in comparison to the other polarization structure functions entering the same asymmetry. Furthermore, one has to take into account that most of the structure functions cannot be measured by one experimental setting. In fact, Table II in Appendix B shows that only six structure functions of a given observable can be obtained from a single asymmetry measurement and only one of the cases discussed in Figs. 11–17 belongs to this list. These considerations show that it is not guaranteed that a specific effect in a structure function will show up in the polarization asymmetry which contains that structure function. In the following we discuss this point in some more detail.

In contrast to the structure functions which depend only on E_{np}, $\vec{q}_{\text{c.m.}}^{\,2}$ and θ, the polarization asymmetries depend in addition on the specific electron, reaction, and orientation kinematics, i.e., on the laboratory electron scattering angle

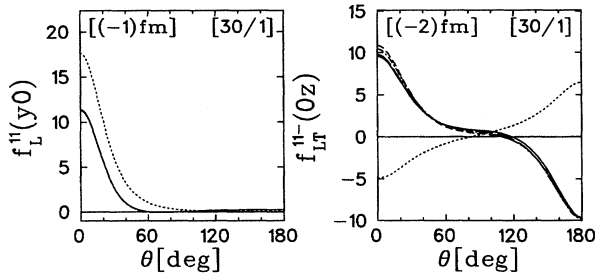

FIG. 11. FSI effect: $f_L^{11}(y0)$ (left) and $f_{LT}^{11-}(0z)$ (right) in the kinematic sector Ia. Notation of the curves as in Fig. 3.

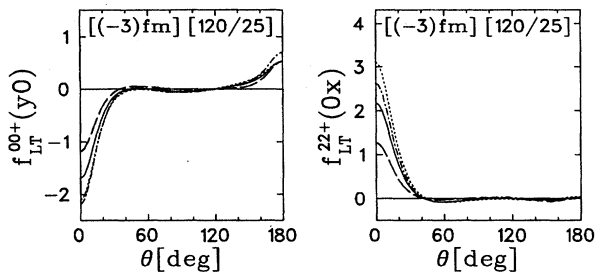

FIG. 13. Potential model dependence: $f_{LT}^{00+}(y0)$ (left) and $f_{LT}^{22+}(0x)$ (right) in the kinematic sector IIc. Notation of the curves as in Fig. 12.

θ_e^{lab}, the azimuthal n-p angle ϕ—the angle between the scattering and reaction planes (see Fig. 2)—and the deuteron orientation angles θ_d and ϕ_d, viz., $\tilde{\phi}=\phi-\phi_d$. These angles are indicated in each of the following figures of the asymmetries in the upper left inset. Furthermore, for a given kinematics we present the asymmetries over a range $0\leq\theta\leq 2\pi$ where for $\pi\leq\theta\leq 2\pi$ we set $f(\theta)=f(\pi-\theta)$ and replace ϕ by $\phi+\pi$ in Eqs. (10)–(15).

We will begin with the simplest case of an unpolarized deuteron target. In Fig. 18 we show two examples, the observables xz and $0x$, where FSI's change dramatically the asymmetry in sector Ia. In $P_0(xz)$ the influence of FSI's leads to a sign change between 60° and 270° and an increase in magnitude while for $P_e(0x)$ the shape is completely altered. The pronounced potential model dependence of $f_{LT}^{00+}(y0)$ at forward angles shown in Figs. 12 and 13 is only reflected in $P_0(y0)$ in Fig. 19 for the sectors IIb/c. Again as in Fig. 13 we see quite similar results between two potential models for the Bonn and Paris potentials on one side and for V_{14} and V_{28} potentials on the other side. This is also observed between 240° and 320°. For quasifree kinematics—sector IIb—the potential model effect at forward angles does not survive because the very large differential cross section S_0 leads to a very small, almost vanishing asymmetry. Very similar results are found for the asymmetries containing the two other structure functions of Figs. 12 and 13.

The effect of subnuclear DOF is demonstrated in Fig. 20. In sector IIIa the influence of IC's is seen most strongly in $P_0(xx)$ near 120° and in $P_e(z0)$ near 240°. Also in the quasifree sector IIb one notices considerable influence from MEC's and IC's in $P_0(y0)$ and $P_0(0z)$, demonstrating the fact that even for quasifree kinematics certain observables are quite sensitive to subnuclear DOF.

Finally we will turn to a few vector and tensor polarization asymmetries where specific effects discussed in Figs. 11–17 are expected to manifest themselves. We begin with the sensitivity to FSI's as seen in Fig. 11 which shows up in the vector asymmetries $P_d^V(y0)$ and $P_d^V(0z)$ in Fig. 21 for the kinematic sector IIa. Here FSI's cause a complete change of pattern in the asymmetry.

MEC and IC effects are demonstrated in Figs. 22 and 23. Figure 22 shows the vector asymmetry $P_d^V(0x)$ and the tensor asymmetry $P_{ed}^T(z0)$. To check a manifestation of the MEC effect of Fig. 14 we have chosen four settings: In the first ones (upper two panels) the structure function under investigation contributes to the asymmetry, while it does not for the settings of the lower two panels. In fact, the MEC effect of Fig. 14 between 0° and 60° is reflected, though somewhat weaker, in the upper part of the figure. However, one also finds MEC effects in a different angular range and,

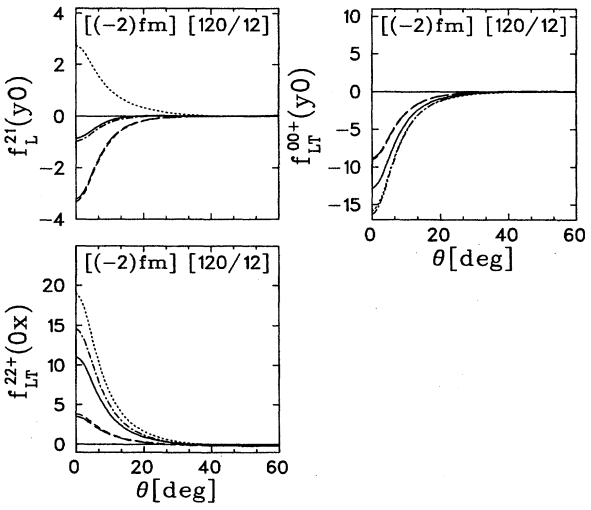

FIG. 12. Potential model dependence: $f_L^{21}(y0)$ (top left), $f_{LT}^{00+}(y0)$ (top right), and $f_{LT}^{22+}(0x)$ (bottom) in the kinematic sector IIb. Notation of the curves: Argonne V_{28} (long dashed line), Argonne V_{14} (short dashed line), Bonn r-space (dotted line), Nijmegen (dash-dotted line), and Paris (solid line).

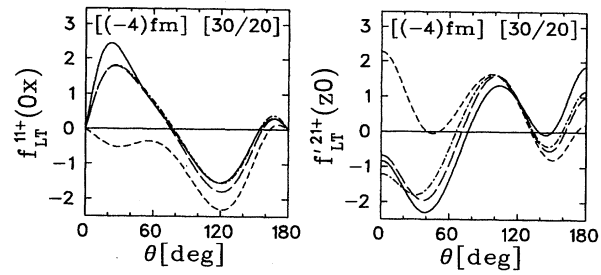

FIG. 14. MEC effect: $f_{LT}^{11+}(0x)$ (left) and $f'^{21+}_{LT}(z0)$ (right) in the kinematic sector Ic. Notation of the curves as in Fig. 3.

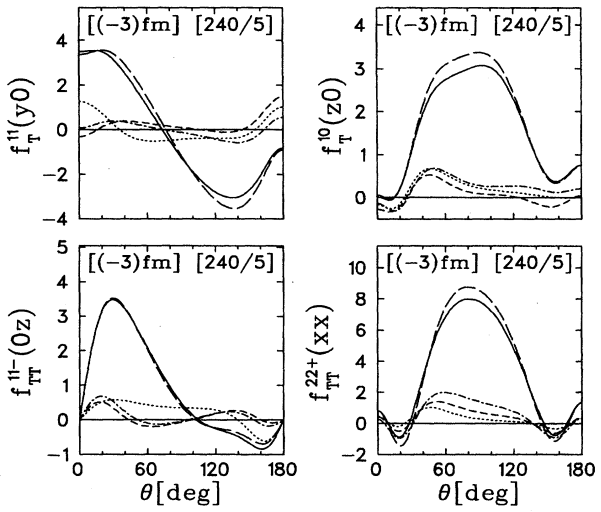

FIG. 15. IC effect: $f_T^{11}(y0)$ (top left), $f_T^{10}(z0)$ (top right), $f_{TT}^{11-}(0z)$ (bottom left), and $f_{TT}^{22+}(xx)$ (bottom right) in the kinematic sector IIIa. Notation of the curves as in Fig. 3.

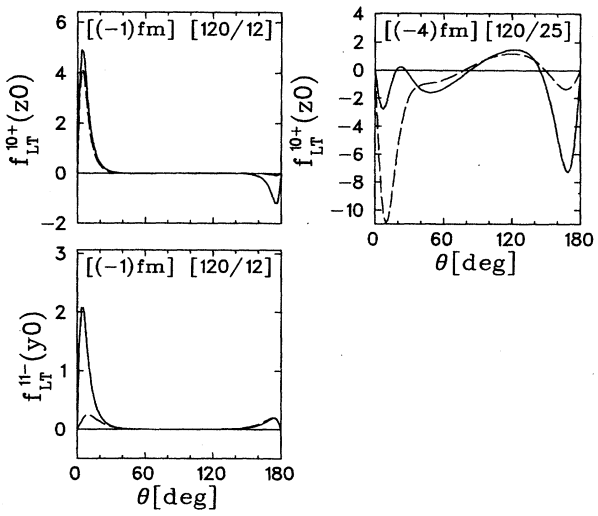

FIG. 17. Relativistic effects: $f_{LT}^{10+}(z0)$ (top) in the kinematic sectors IIb and IIc and $f_{LT}^{11-}(y0)$ (bottom) in the kinematic sector IIb. Notation of the curves: N+MEC+IC (long dashed line) and additional RC's (solid line).

moreover, strong MEC effects are also present for the asymmetry in the lower left panel. This illustrates the fact that a specific effect in one structure function is not always reflected in the corresponding asymmetry. The reason for this is on the one hand the subtle interplay between several structure functions which contribute to the numerator of a polarization asymmetry and, on the other hand, the influence of the differential cross section in the denominator which also changes with the choice of the angles ϕ, θ_d and ϕ_d.

The strong IC effects of Fig. 15 are also reflected in Fig. 23 in the tensor asymmetry $P_d^T(xx)$ and the vector asymmetry $P_d^V(z0)$ in sector IIIa. For $P_d^T(xx)$ we show two different settings of the deuteron orientation angle θ_d in order to demonstrate again the dependence on this angle. For $\theta_d=0°$ the largest effect appears near 120° and near 300°. However, one has to be aware that f_{TT}^{22} of Fig. 15 does not contribute to this asymmetry, while it does for the second setting ($\theta_d=90°$). Therefore it is not surprising that one finds in the second case an even more pronounced IC effect which is situated between 220° and 300°. The vector asymmetry $P_d^V(z0)$ exhibits an even stronger influence of IC's over a large angular range originating from the strong IC dependence of $f_T^{10}(z0)$ in Fig. 15.

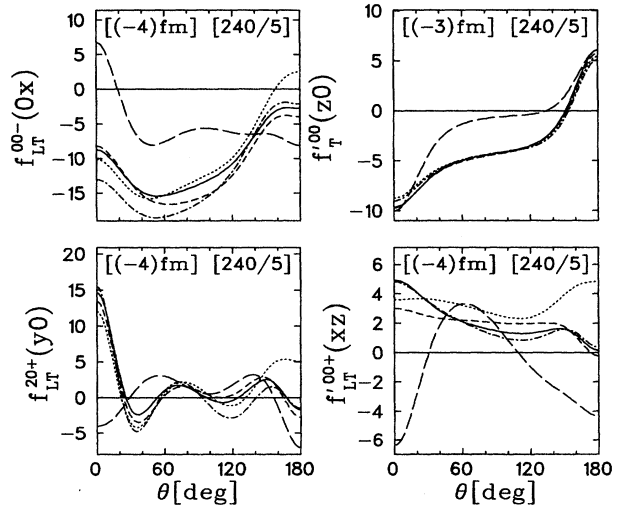

FIG. 16. Comparison of IC effect in IA to coupled channel calculation with V_{28}: $f_{LT}^{00-}(0x)$ (top left), $f'^{00}_T(z0)$ (top right), $f_{LT}^{20+}(y0)$ (bottom left), and $f'^{00+}_{LT}(xz)$ (bottom right) in the kinematic sector IIIa. Notation of the curves as in Fig. 12.

The different treatment of IC's in the IA or CC approach which shows up in the structure functions in Fig. 16 gives a strong signal also in $P_0(0x)$ and $P_e(z0)$ and in the tensor asymmetry $P_d^T(y0)$ in Fig. 24. Particularly striking is $P_e(z0)$ where all potential models give essentially the same result in the IA whereas for the other two cases one notes a larger variation also for the IA, but still distinctly different from the CC approach.

Relativistic effects are in general less conspicuous than the subnuclear ones. The relatively largest signatures are found in small asymmetries, making their detection more difficult. We present in Fig. 25 a few examples of vector and tensor asymmetries which are not too small but still show sizable influence from RC's. The vector asymmetry $P_d^V(z0)$ reaches almost ±40% in sector Ic and is quite sensitive to RC's over the whole angular range while $P_d^V(y0)$ is slightly smaller but still showing significant RC effects. The tensor asymmetries in sector IIc are even smaller, of the order of 10%. Particularly large changes from RC's are seen in $P_d^T(0z)$ near 90° and 240° whereas $P_d^T(z0)$ exhibits much smaller sensitivity to RC's.

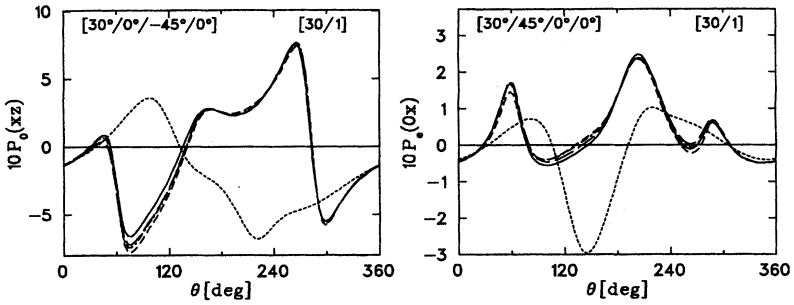

FIG. 18. Influence of FSI's on the polarization asymmetries $P_0(xz)$ (left) and $P_e(0x)$ (right) for an unpolarized deuteron target in sector Ia. The top left inset "$[\theta_e^{\rm lab}/\phi/\tilde{\phi}/\theta_d]$" indicates the chosen laboratory electron scattering angle $\theta_e^{\rm lab}$, the c.m. n-p angle ϕ, the deuteron orientation angle θ_d, and $\tilde{\phi}=\phi-\phi_d$ on which the asymmetries depend. The top right inset indicates as before the kinematic sector. Notation of the curves as in Fig. 3.

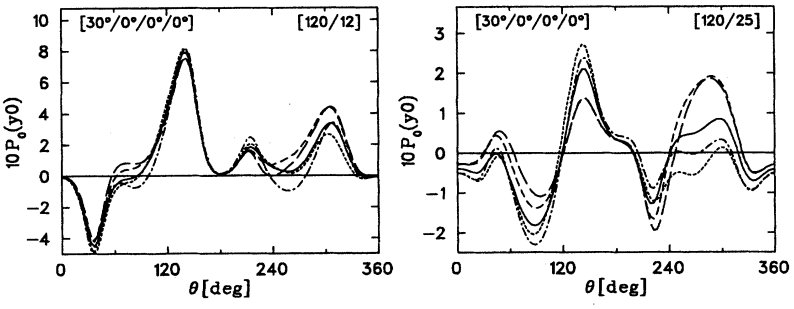

FIG. 19. Potential model dependence of $P_0(y0)$ in the kinematic sectors IIb/c. Notation of the curves as in Fig. 12. For the meaning of the upper left inset see Fig. 18.

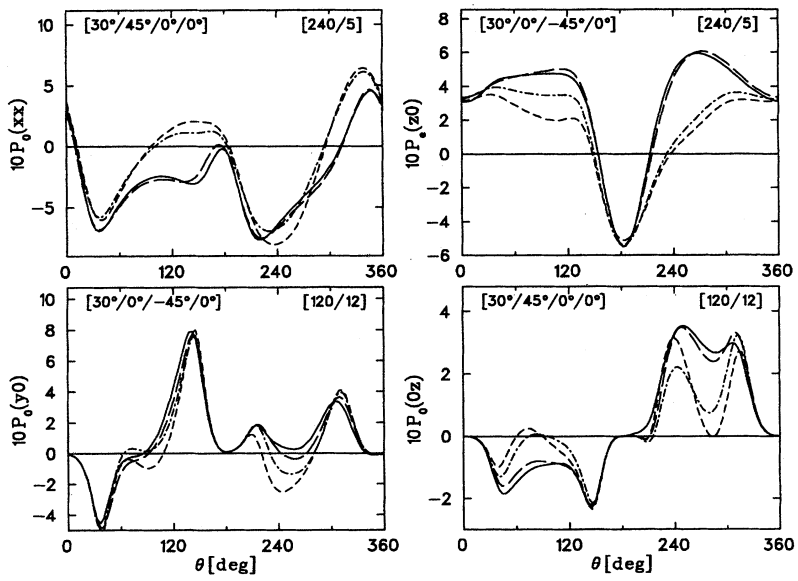

FIG. 20. Influence of subnuclear DOF on the asymmetries $P_0(xx)$ (top left), $P_e(z0)$ (top right), $P_0(y0)$ (bottom left), and $P_0(0z)$ (bottom right) for an unpolarized deuteron target in sectors IIb and IIIa. Notation of the curves as in Fig. 3. For the meaning of the upper left inset see Fig. 18.

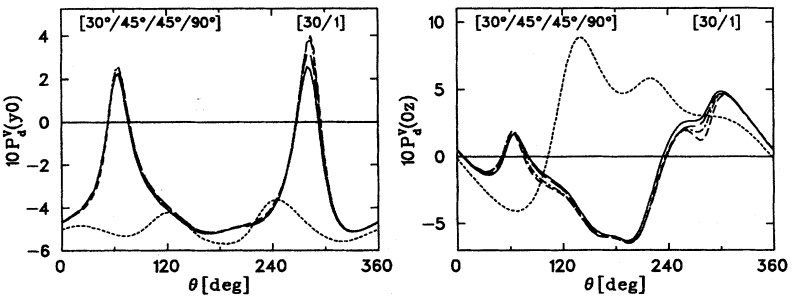

FIG. 21. Influence of FSI's on the vector polarization asymmetries $P_d^V(y0)$ (left) and $P_d^V(0z)$ (right) in sector Ia. Notation of the curves as in Fig. 3. For the meaning of the upper left inset see Fig. 18.

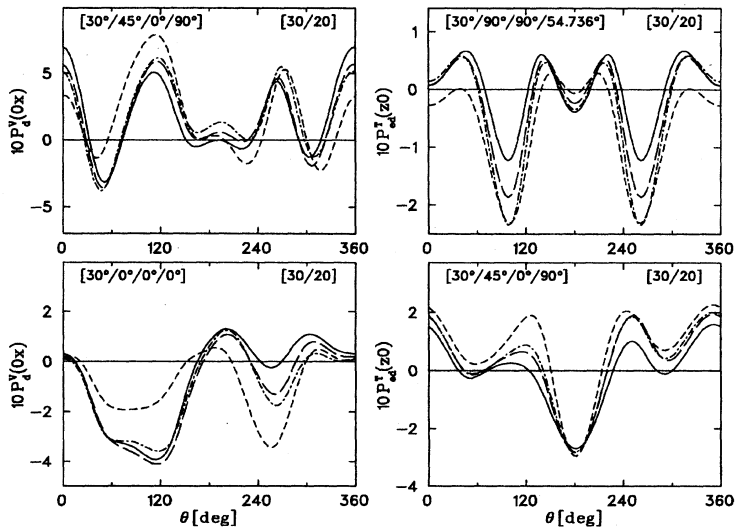

FIG. 22. Influence of MEC's on the vector polarization asymmetry $P_d^V(0x)$ (top and bottom left) and the tensor asymmetry $P_{ed}^T(z0)$ (top and bottom right) in sector Ic, each for two different kinematic settings of the angles. Notation of the curves as in Fig. 3. For the meaning of the upper left inset see Fig. 18.

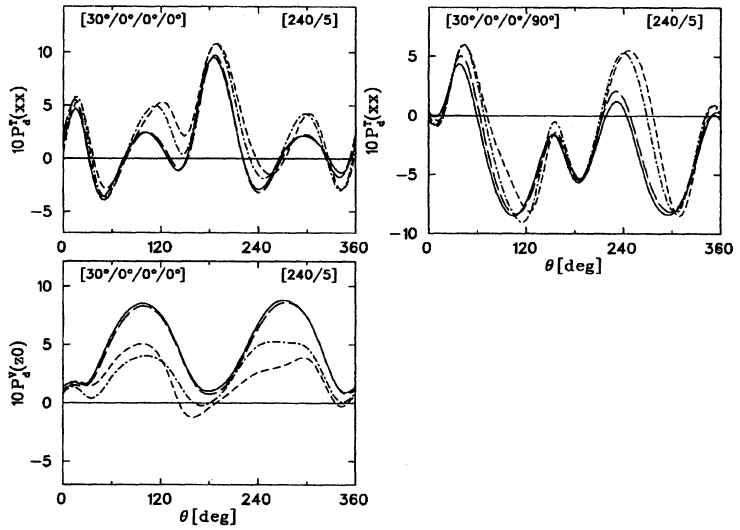

FIG. 23. Influence of IC's on the tensor asymmetry $P_d^T(xx)$ (top) and the vector asymmetry $P_d^V(z0)$ (bottom) in the kinematic sector IIIa. Notation of the curves as in Fig. 3. For the meaning of the upper left inset see Fig. 18.

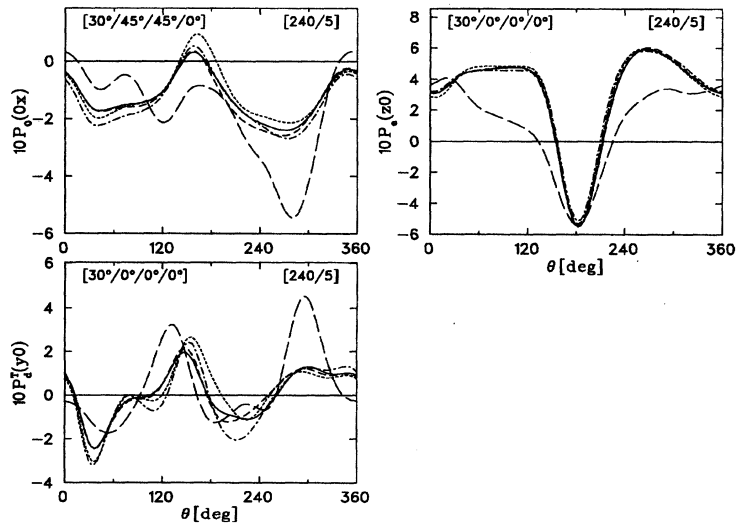

FIG. 24. Comparison of IC effects in the IA to a coupled channel calculation with V_{28}: tensor asymmetry $P_0(0x)$ (top left), $P_e(z0)$ (top right), and $P_d^T(y0)$ (bottom) in the kinematic sector IIIa. Notation of the curves as in Fig. 12. For the meaning of the upper left inset see Fig. 18.

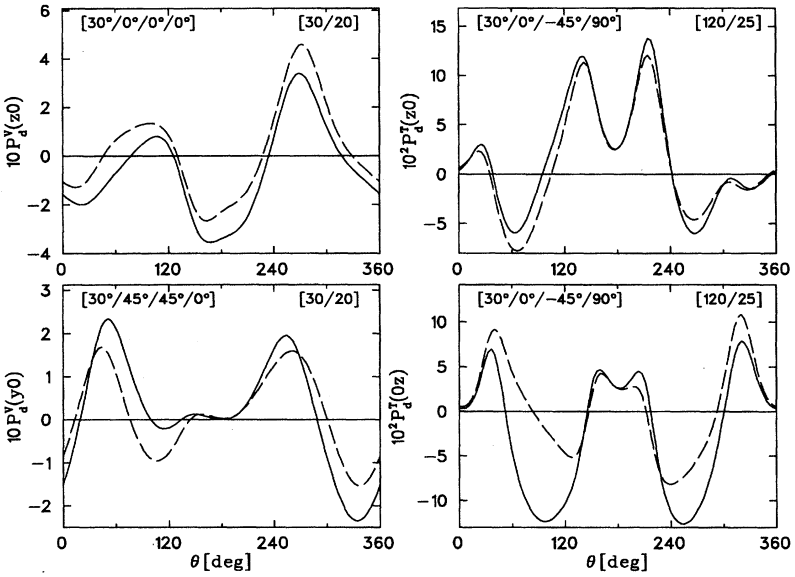

FIG. 25. Influence of RC's on the vector asymmetries $P_d^V(z0)$ (top left) and $P_d^V(y0)$ (bottom left), and the tensor asymmetries $P_d^T(z0)$ (top right) and $P_d^T(0z)$ (bottom right) in the kinematic sectors Ic and IIc, respectively. Notation of the curves as in Fig. 17. For the meaning of the upper left inset see Fig. 18.

Finally we would like to briefly discuss the influence of the neutron electric form factor G_{En} on the asymmetries. In addition to the well-known asymmetries $P_e(0x)$ and A_{ed}^V Mosconi *et al.* [13] have found the vector asymmetry $P_d^V(0z)$ and the tensor asymmetry $P_{ed}^T(x0)$ to be very sensitive to G_{En} at forward neutron emission and for $\theta_d=90°$ and $\phi_d=0°$. The sensitivity of the vector asymmetry $P_d^V(0z)$ to G_{En} is not really surprising since all observables of the elementary electron-nucleon scattering process which are sensitive to the interference of G_E and G_M involve either virtual-photon-target spin correlations or spin transfer from the virtual photon or target nucleon to the final nucleon always for the x and z components which lie in the scattering plane. For example, $P_e(0x)$ involves the spin transfer $P_z(\gamma^*)\rightarrow P_x(n)$ and the vector-target-beam asymmetry A_{ed}^V [9] involves the spin correlation between $P_z(\gamma^*)$ and $P_x(n)$ of the target neutron since a vector polarized deuteron corresponds to a polarized neutron target. Similarly, $P_d^V(0z)$ with $\theta_d=90°$ describes the spin transfer $P_x(n)\rightarrow P_z(n)$. Thus it is not surprising that we have found another asymmetry which shows a similar strong influence from G_{En}, namely, the vector asymmetry $P_d^V(0x)$ for $\theta_d=0°$ corresponding to the inverse spin transfer $P_z(n)\rightarrow P_x(n)$. In addition we have found six more asymmetries which show a significant influence from G_{En}. All of them involve spin correlations between x and z components of the outgoing proton and neutron, namely, two asymmetries for an unpolarized deuteron $P_0(xz)$ and $P_0(zx)$, two

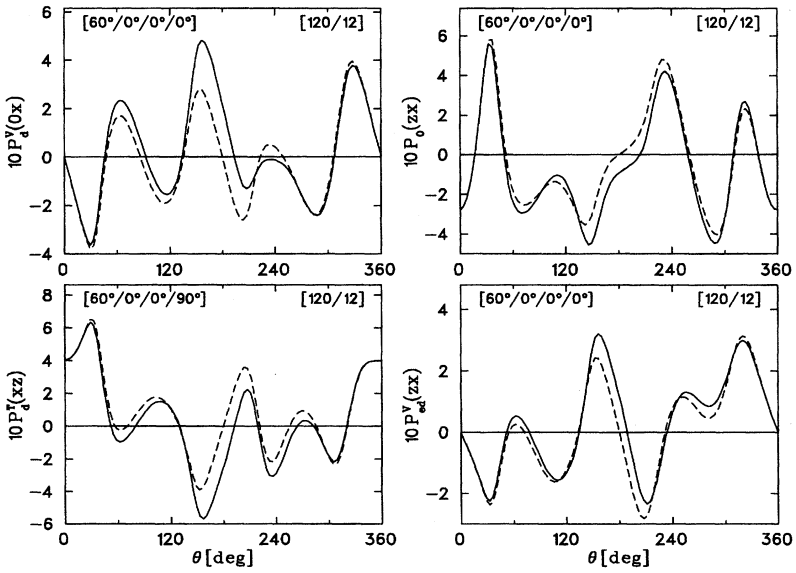

FIG. 26. Influence of G_{En} on various asymmetries in the kinematic sector IIb. Notation of the curves: $G_{En}=0$ (dashed line) and $G_{En}\neq 0$ (solid line). For the meaning of the upper left inset see Fig. 18.

vector asymmetries $P_{ed}^{V}(zx)$ ($\theta_d=0°$) and $P_{ed}^{V}(xx)$ ($\theta_d=90°$), and two tensor asymmetries $P_d^T(xz)$ and $P_d^T(zx)$. We show in Fig. 26 the vector asymmetry $P_d^V(0x)$ as well as three of the more complicated ones. Indeed, one sees in the direction of forward neutron emission ($\theta=180°$) the large change from practically zero for $G_{En}=0$ to a substantial nonzero value for $G_{En}\neq 0$. However, the sensitivity to G_{En} is only useful for a study of G_{En} if all the other effects are minimal. In fact, we have checked that MEC, IC, and RC contributions and potential model dependences vanish in the interesting kinematical region for all of the above mentioned asymmetries. However, only $P_d^V(0x)$, like $P_d^V(0z)$, is of particular interest because all the other mentioned observables are too difficult to measure. Both of them can be considered as real alternatives to the measurement of $P_e(0x)$.

This concludes the last part of our systematic study of polarization effects in deuteron electrodisintegration considering beam and target polarization and analysis of the outgoing nucleon polarization. We have shown that various interesting effects related to the NN potential, to subnuclear DOF in terms of MEC's and IC's, and to relativistic contributions and the neutron electric form factor may be studied in great detail in a variety of kinematic regions with respect to energy and momentum transfer. We hope that this study will serve a twofold purpose, both as a stimulus and a guideline for future experimental studies of this fundamental and interesting process.

ACKNOWLEDGMENTS

This work is partially supported by the Deutsche Forschungsgemeinschaft (SFB 201) and by the National Science and Engineering Research Council of Canada. In addition the authors collectively acknowledge the hospitality and support of the Saskatchewan Accelerator Laboratory, the University of Trento, the European Centre for Theoretical Studies in Nuclear Physics and Related Areas (Trento), and the Institut für Kernphysik (Mainz).

APPENDIX A: STRUCTURE FUNCTIONS

Here we will list the explicit expressions for the various structure functions in terms of the t-matrix elements $t_{sm_s\lambda m}$:

$$f_L^{IM}(X)=\frac{2}{1+\delta_{M0}}\Re(i^{\tilde{\delta}_I^X}\mathscr{C}_X^{00IM}) , \tag{A1}$$

$$f_T^{IM}(X)=\frac{4}{1+\delta_{M0}}\Re(i^{\tilde{\delta}_I^X}\mathscr{C}_X^{11IM}) , \tag{A2}$$

$$f_{LT}^{IM\pm}(X)=\frac{4}{1+\delta_{M0}}\Re[i^{\tilde{\delta}_I^X}(\mathscr{C}_X^{01IM} \pm(-)^{I+M+\delta_{X,\,B}}\mathscr{C}_X^{01I-M})] , \tag{A3}$$

$$f_{TT}^{IM\pm}(X)=\frac{2}{1+\delta_{M0}}\Re[i^{\tilde{\delta}_I^X}(\mathscr{C}_X^{-11IM} \pm(-)^{I+M+\delta_{X,\,B}}\mathscr{C}_X^{-11I-M})] , \tag{A4}$$

$$f_T'^{IM}(X)=\frac{4}{1+\delta_{M0}}\Re(i^{1+\tilde{\delta}_I^X}\mathscr{C}_X^{11IM}) , \tag{A5}$$

$$f_{LT}'^{IM\pm}(X)=\frac{4}{1+\delta_{M0}}\Re[i^{1+\tilde{\delta}_I^X}(\mathscr{C}_X^{01IM} \pm(-)^{I+M+\delta_{X,\,B}}\mathscr{C}_X^{01I-M})] . \tag{A6}$$

Specifying the observable X, one has the following in detail.

(i) Differential cross section ($X=1$)

$$\mathscr{C}_1^{\lambda'\lambda IM}=\sum_s \hat{s}u_{\lambda'\lambda IM}^{ss00} . \tag{A7}$$

(ii) Single-nucleon polarization

$$\mathscr{C}_{x(1)}^{\lambda'\lambda IM}=-\sqrt{\tfrac{3}{2}}(V_{\lambda'\lambda IM}^{1011}-V_{\lambda'\lambda IM}^{101-1}) , \tag{A8}$$

$$\mathscr{C}_{x(2)}^{\lambda'\lambda IM}=-\sqrt{\tfrac{3}{2}}(V_{\lambda'\lambda IM}^{0111}-V_{\lambda'\lambda IM}^{011-1}) , \tag{A9}$$

$$\mathscr{C}_{y(1)}^{\lambda'\lambda IM}=i\sqrt{\tfrac{3}{2}}(V_{\lambda'\lambda IM}^{1011}+V_{\lambda'\lambda IM}^{101-1}) , \tag{A10}$$

$$\mathscr{C}_{y(2)}^{\lambda'\lambda IM}=i\sqrt{\tfrac{3}{2}}(V_{\lambda'\lambda IM}^{0111}+V_{\lambda'\lambda IM}^{011-1}) , \tag{A11}$$

$$\mathscr{C}_{z(1)}^{\lambda'\lambda IM}=\sqrt{3}V_{\lambda'\lambda IM}^{1010} , \tag{A12}$$

$$\mathscr{C}_{z(2)}^{\lambda'\lambda IM}=\sqrt{3}V_{\lambda'\lambda IM}^{0110} , \tag{A13}$$

where

$$V_{\lambda'\lambda IM}^{101\sigma}=\sqrt{2}\sum_{s's}(-)^s\hat{s}'\hat{s}\begin{Bmatrix} s' & s & 1 \\ \frac{1}{2} & \frac{1}{2} & \frac{1}{2}\end{Bmatrix}u_{\lambda'\lambda IM}^{s's1\sigma} , \tag{A14}$$

$$V_{\lambda'\lambda IM}^{011\sigma}=\sqrt{2}\sum_{s's}(-)^{s'}\hat{s}'\hat{s}\begin{Bmatrix} s' & s & 1 \\ \frac{1}{2} & \frac{1}{2} & \frac{1}{2}\end{Bmatrix}u_{\lambda'\lambda IM}^{s's1\sigma} . \tag{A15}$$

(iii) Double-nucleon polarization

$$\mathscr{C}_{xx/yy}^{\lambda'\lambda IM}=-\sqrt{3}\left[V_{\lambda'\lambda IM}^{1100}+\frac{1}{\sqrt{2}}V_{\lambda'\lambda IM}^{1120} \mp\frac{\sqrt{3}}{2}(V_{\lambda'\lambda IM}^{1122}+V_{\lambda'\lambda IM}^{112-2})\right] , \tag{A16}$$

$$\mathscr{C}_{zz}^{\lambda'\lambda IM}=-\sqrt{3}[V_{\lambda'\lambda IM}^{1100}-\sqrt{2}V_{\lambda'\lambda IM}^{1120}] , \tag{A17}$$

$$\mathscr{C}_{xy/yx}^{\lambda'\lambda IM}=-\frac{3i}{2}[\pm\sqrt{2}V_{\lambda'\lambda IM}^{1110}+(V_{\lambda'\lambda IM}^{1122}-V_{\lambda'\lambda IM}^{112-2})] , \tag{A18}$$

$$\mathscr{U}^{\lambda'\lambda IM}_{xz/zx} = -\tfrac{3}{2}[\pm(V^{1111}_{\lambda'\lambda IM}+V^{111-1}_{\lambda'\lambda IM})+(V^{1121}_{\lambda'\lambda IM}-V^{112-1}_{\lambda'\lambda IM})]\ , \tag{A19}$$

$$\mathscr{U}^{\lambda'\lambda IM}_{yz/zy} = \frac{3i}{2}[\pm(V^{1111}_{\lambda'\lambda IM}-V^{111-1}_{\lambda'\lambda IM})+(V^{1121}_{\lambda'\lambda IM}+V^{112-1}_{\lambda'\lambda IM})]\ , \tag{A20}$$

where the quantities $V^{\tau'\tau S\sigma}_{\lambda'\lambda IM}$ are given by

$$V^{\tau'\tau S\sigma}_{\lambda'\lambda IM} = 2\hat{S}\sum_{s's}\hat{s}'\hat{s}\begin{Bmatrix} \frac{1}{2} & \frac{1}{2} & \tau' \\ \frac{1}{2} & \frac{1}{2} & \tau \\ s' & s & S \end{Bmatrix} u^{s's S\sigma}_{\lambda'\lambda IM}\ , \tag{A21}$$

and

$$u^{s's S\sigma}_{\lambda'\lambda IM} = \hat{I}\sqrt{3}\sum_{m_{s'}m_s m'm}(-)^{1-m+s'-m_{s'}}\begin{pmatrix} 1 & 1 & I \\ m' & -m & M \end{pmatrix}\begin{pmatrix} s' & s & S \\ m_{s'} & -m_s & -\sigma \end{pmatrix} t^*_{s'm_{s'}\lambda'm'}t_{sm_s\lambda m}\ . \tag{A22}$$

APPENDIX B: SEPARATION OF STRUCTURE FUNCTIONS

In Ref. [2] we showed how the various structure functions of an A-type observable could be determined from measurements of the appropriate asymmetry. There we restricted our considerations to the nonpreviously discussed $I>0$ structure functions. In some cases the structure function could be determined from a single asymmetry measurement while others required two or more measurements. However, we missed the optimal number of measurements for some of the structure functions. In fact a few of them require fewer settings than given in Ref. [2]. Two can be obtained with four instead of six settings (f^{21+}_{TT}, f^{22+}_{TT}), while three others can be determined by two instead of four settings (f^{21+}_{LT}, f^{22+}_{LT}, $f'^{\,22-}_{LT}$). For the three latter cases the expressions are as follows with $\cos\theta^0_d = 1/\sqrt{3}$:

$$\rho_{LT}f^{21+}_{LT}(X) = \sqrt{\frac{3}{2}}\left[S^T_d\left(X;\pi,\frac{\pi}{4},\theta^0_d\right)-S^T_d\left(X;0,\frac{\pi}{4},\theta^0_d\right)\right]\ , \tag{B1}$$

$$\rho_{LT}f^{22+}_{LT}(X) = \sqrt{\frac{3}{2}}\left[S^T_d\left(X;\pi,\frac{\pi}{2},\theta^0_d\right)-S^T_d\left(X;0,\frac{\pi}{2},\theta^0_d\right)\right]\ , \tag{B2}$$

$$\rho_{LT'}f'^{\,22-}_{LT}(X) = \sqrt{\frac{2}{3}}\left[S^T_{ed}\left(X;0,\frac{\pi}{4},\frac{\pi}{2}\right)-S^T_{ed}\left(X;\pi,\frac{\pi}{4},\frac{\pi}{2}\right)\right]\ , \tag{B3}$$

where we adopt the same convenient notation as used previously,

$$S^{V/T}_{d/ed}(X;\phi,\tilde{\phi},\theta_d) = \frac{1}{c}\,S_0(\phi)P^{V/T}_{d/ed}(X;\phi,\tilde{\phi},\theta_d)\ . \tag{B4}$$

Now we turn to the separation of structure functions for B-type observables using the expressions (10)–(15). Without target and electron polarization one has two structure functions which can be determined by one (f^{00-}_{LT}, $\phi=\pi/2$) and two (f^{00-}_{LT}, $\phi=\pi/4,\pi/2$) out-of-plane measurements. Electron polarization only leads to two other structure functions: $f'^{\,00-}_{LT}$ which can be obtained from one out-of-plane measurement at $\phi=\pi/2$, and $f'^{\,00}_{T}$ which requires two settings.

For the structure functions with target polarization we find that six of them can be determined by a single asymmetry measurement. They are

$$\rho_{LT}f^{11-}_{LT}(X) = \sqrt{2}S^V_d\left(X;\frac{\pi}{2},\frac{\pi}{2},\frac{\pi}{2}\right)\ , \tag{B5}$$

$$\rho_{LT}f^{20-}_{LT}(X) = S^T_d\left(X;\frac{\pi}{2},\tilde{\phi},0\right)\ , \tag{B6}$$

$$\rho'_Tf'^{\,11}_T(X) = -\sqrt{2}S^V_{ed}\left(X;\frac{\pi}{2},\frac{\pi}{2},\frac{\pi}{2}\right)\ , \tag{B7}$$

$$\rho'_Tf'^{\,20}_T(X) = -S^T_{ed}\left(X;\frac{\pi}{2},\tilde{\phi},0\right)\ , \tag{B8}$$

$$\rho'_{LT}f'^{\,10+}_{LT}(X) = S^V_{ed}\left(X;\frac{\pi}{2},\tilde{\phi},0\right)\ , \tag{B9}$$

$$\rho'_{LT}f'^{\,11+}_{LT}(X) = -\sqrt{2}S^V_{ed}\left(X;\frac{\pi}{2},0,\frac{\pi}{2}\right)\ . \tag{B10}$$

Sixteen other structure functions require only two measurements for their separation. These are

$$\rho_{LT}f^{10+}_{LT}(X) = \frac{1}{\sqrt{2}}\left[S^V_d\left(X;\frac{\pi}{4},\tilde{\phi},0\right)-S^V_d\left(X;\frac{3\pi}{4},\tilde{\phi},0\right)\right]\ , \tag{B11}$$

$$\rho_{LT}f^{11+}_{LT}(X) = -\left[S^V_d\left(X;\frac{\pi}{4},0,\frac{\pi}{2}\right)-S^V_d\left(X;\frac{3\pi}{4},0,\frac{\pi}{2}\right)\right]\ , \tag{B12}$$

$$\rho_{LT} f_{LT}^{21+}(X) = \sqrt{\frac{2}{3}}\left[S_d^T\left(X;\pi,\frac{\pi}{2},\frac{\pi}{4}\right) - S_d^T\left(X;0,\frac{\pi}{2},\frac{\pi}{4}\right)\right], \tag{B13}$$

$$\rho_{LT} f_{LT}^{21-}(X) = -\sqrt{\frac{2}{3}}\left[S_d^T\left(X;\frac{\pi}{2},0,\frac{\pi}{4}\right) - S_d^T\left(X;\frac{\pi}{2},0,\frac{3\pi}{4}\right)\right], \tag{B14}$$

$$\rho_{LT} f_{LT}^{22+}(X) = \sqrt{\frac{2}{3}}\left[S_d^T\left(X;0,\frac{\pi}{4},\frac{\pi}{2}\right) - S_d^T\left(X;\pi,\frac{\pi}{4},\frac{\pi}{2}\right)\right], \tag{B15}$$

$$\rho_{LT} f_{LT}^{22-}(X) = 2\sqrt{\frac{2}{3}}\left[S_d^T\left(X;\frac{\pi}{2},0,\frac{\pi}{2}\right) + \frac{1}{2} S_d^T\left(X;\frac{\pi}{2},\tilde{\phi},0\right)\right], \tag{B16}$$

$$\rho_{TT} f_{TT}^{11-}(X) = -S_d^V\left(X;\frac{\pi}{2},\frac{\pi}{2},\frac{\pi}{2}\right) + \sqrt{2} S_d^V\left(X;\frac{\pi}{4},\frac{\pi}{2},\frac{\pi}{2}\right), \tag{B17}$$

$$\rho_{TT} f_{TT}^{20-}(X) = S_d^T\left(X;\frac{\pi}{4},\tilde{\phi},0\right) - \frac{1}{\sqrt{2}} S_d^T\left(X;\frac{\pi}{2},\tilde{\phi},0\right), \tag{B18}$$

$$\rho_T' f_T'^{21}(X) = \sqrt{\frac{3}{2}}\left[S_{ed}^T\left(X;0,\frac{\pi}{4},\theta_d^0\right) + S_{ed}^T\left(X;\pi,\frac{\pi}{4},\theta_d^0\right)\right], \tag{B19}$$

$$\rho_T' f_T'^{22}(X) = \sqrt{\frac{3}{2}}\left[S_{ed}^T\left(X;0,\frac{\pi}{2},\theta_d^0\right) + S_{ed}^T\left(X;\pi,\frac{\pi}{2},\theta_d^0\right)\right], \tag{B20}$$

$$\rho_{LT}' f_{LT}'^{11-}(X) = -\sqrt{2}\left[S_{ed}^V\left(X;0,\frac{\pi}{2},\frac{\pi}{2}\right) - S_{ed}^V\left(X;\frac{\pi}{2},\frac{\pi}{2},\frac{\pi}{2}\right)\right], \tag{B21}$$

$$\rho_{LT}' f_{LT}'^{20-}(X) = S_{ed}^T\left(X;\frac{\pi}{2},\tilde{\phi},0\right) - S_{ed}^T(X;0,\tilde{\phi},0), \tag{B22}$$

$$\rho_{LT}' f_{LT}'^{21+}(X) = -\sqrt{\frac{2}{3}}\left[S_{ed}^T\left(X;\frac{\pi}{2},\frac{\pi}{2},\frac{\pi}{4}\right) - S_{ed}^T\left(X;\frac{\pi}{2},\frac{\pi}{2},\frac{3\pi}{4}\right)\right], \tag{B23}$$

$$\rho_{LT}' f_{LT}'^{21-}(X) = \sqrt{\frac{3}{2}}\left[S_{ed}^T\left(X;0,\frac{\pi}{4},\theta_d^0\right) - S_{ed}^T\left(X;\pi,\frac{\pi}{4},\theta_d^0\right)\right], \tag{B24}$$

$$\rho_{LT}' f_{LT}'^{22+}(X) = \sqrt{\frac{2}{3}}\left[2S_{ed}^T\left(X;\frac{\pi}{2},\frac{\pi}{4},\frac{\pi}{2}\right) + S_{ed}^T\left(X;\frac{\pi}{2},\tilde{\phi},0\right)\right], \tag{B25}$$

$$\rho_{LT}' f_{LT}'^{22-}(X) = \sqrt{\frac{3}{2}}\left[S_{ed}^T\left(X;0,\frac{\pi}{2},\theta_d^0\right) - S_{ed}^T\left(X;\pi,\frac{\pi}{2},\theta_d^0\right)\right]. \tag{B26}$$

In this last set of equations as well as for what follows we have made a choice of angles to effect the separations. This choice is not unique and other choices will lead to different coefficients in the linear combinations. The terms $\rho_L f_L^{10}(X) + \rho_T f_T^{10}(X)$ and $\rho_L f_L^{11}(X) + \rho_T f_T^{11}(X)$ in $P_d^V(X)$ can also be determined from two asymmetry measurements, i.e.,

$$\rho_L f_L^{10}(X) + \rho_T f_T^{10}(X) = \frac{1}{2}\left[S_d^V\left(X;\frac{\pi}{4},\tilde{\phi},0\right) + S_d^V\left(X;\frac{3\pi}{4},\tilde{\phi},0\right)\right], \tag{B27}$$

$$\rho_L f_L^{11}(X) + \rho_T f_T^{11}(X) = -\frac{1}{\sqrt{2}}\left[S_d^V\left(X;\frac{\pi}{4},0,\frac{\pi}{2}\right) + S_d^V\left(X;\frac{3\pi}{4},0,\frac{\pi}{2}\right)\right]. \tag{B28}$$

In order to separate the longitudinal from the transverse part one needs in addition a Rosenbluth analysis.

Increasing the number of asymmetry measurements to 3 allows one to determine only two further structure functions, namely,

$$\rho_{TT} f_{TT}^{11+}(X) = -\frac{1}{\sqrt{2}}\left[S_d^V\left(X;\frac{\pi}{4},0,\frac{\pi}{2}\right) + S_d^V\left(X;\frac{3\pi}{4},0,\frac{\pi}{2}\right) - 2S_d^V\left(X;\frac{\pi}{2},0,\frac{\pi}{2}\right)\right], \tag{B29}$$

$$\rho_{TT} f_{TT}^{10+}(X) = \frac{1}{2}\left[S_d^V\left(X;\frac{\pi}{4},\tilde{\phi},0\right) + S_d^V\left(X;\frac{3\pi}{4},\tilde{\phi},0\right)\right] - S_d^V\left(X;\frac{\pi}{2},\tilde{\phi},0\right). \tag{B30}$$

Three settings also allow a determination of the combination

$$\rho_L f_L^{22}(X) + \rho_T f_T^{22}(X) = \sqrt{\frac{2}{3}}\left[S_d^T\left(X;\frac{\pi}{4},\frac{\pi}{4},\frac{\pi}{2}\right) + S_d^T\left(X;\frac{3\pi}{4},\frac{\pi}{4},\frac{\pi}{2}\right) + \frac{1}{\sqrt{2}} S_d^T\left(X;\frac{\pi}{2},\tilde{\phi},0\right)\right]. \tag{B31}$$

All 14 vector structure functions and 16 of the tensor ones are then determined. For the remaining functions $f_{TT}^{21+}(X)$, $f_{TT}^{21-}(X)$, $f_{TT}^{22+}(X)$, $f_{TT}^{22-}(X)$, and $[\rho_L f_L^{21}(X) + \rho_T f_T^{21}(X)]$ one needs four measurements in order to determine them. The last combination and the one in (B31) require an additional Rosenbluth separation. A survey on the number of asymmetry measurements needed for the separation of a given structure function is given in Table II.

TABLE II. Number of asymmetry measurements for a structure function of an observable X. The symbol (R) indicates the need of an additional Rosenbluth L-T separation.

				$X \in A$				
IM	*L, T*	*LT+*	*LT−*	*TT+*	*TT−*	*T′*	*LT′+*	*LT′−*
10	–	–	1	–	2	1	–	2
11	2(R)	2	1	3	2	1	1	2
20	2(R)	2	–	3	–	–	1	–
21	4(R)	2	2	4	4	2	2	2
22	4(R)	2	2	4	4	2	2	2
				$X \in B$				
IM	*L, T*	*LT+*	*LT−*	*TT+*	*TT−*	*T′*	*LT′+*	*LT′−*
10	2(R)	2	–	3	–	–	1	–
11	2(R)	2	1	3	2	1	1	2
20	–	–	1	–	2	1	–	2
21	4(R)	2	2	4	4	2	2	2
22	3(R)	2	2	4	4	2	2	2

[1] W. Leidemann, E.L. Tomusiak, and H. Arenhövel, Phys. Rev. C **43**, 1022 (1990).

[2] H. Arenhövel, W. Leidemann, and E.L. Tomusiak, Phys. Rev. C **46**, 455 (1992).

[3] H. Arenhövel, W. Leidemann, and E.L. Tomusiak, Few-Body Syst. **15**, 109 (1993).

[4] H. Arenhövel, Few-Body Syst. **4**, 55 (1988).

[5] H. Arenhövel and K.-M. Schmitt, Few-Body Syst. **8**, 77 (1990).

[6] V. Dmitrasinovic and F. Gross, Phys. Rev. C **40**, 2479 (1989).

[7] W. Fabian and H. Arenhövel, Nucl. Phys. **A314**, 253 (1979).

[8] H. Arenhövel, Phys. Lett. B **199**, 13 (1987).

[9] H. Arenhövel, W. Leidemann, and E.L. Tomusiak, Z. Phys. A **331**, 123 (1988); **334**, 363(E) (1989).

[10] A.Yu. Korchin, Yu.P. Mel'nik, and A.V. Shebeko, Few-Body Syst. **9**, 211 (1990).

[11] Yu.P. Mel'nik and A.V. Shebeko, Few-Body Syst. **13**, 59 (1992).

[12] T. Wilbois, G. Beck, and H. Arenhövel, Few-Body. Syst. **15**, 39 (1993).

[13] B. Mosconi, J. Pauschenwein, and P. Ricci, Phys. Rev. C **48**, 332 (1993).

[14] B.A. Robson, *The Theory of Polarization Phenomena* (Clarendon Press, Oxford, 1974).

[15] F. Partovi, Ann. Phys. (N.Y.) **27**, 79 (1964).

[16] M.M. Nagels, T.A. Rijken, and J.J. de Swart, Phys. Rev. D **17**, 768 (1978).

[17] M. Lacombe, B. Loiseau, J.M. Richard, R. Vinh Mau, J. Côté,

P. Pirès, and R. de Tourreil, Phys. Rev. C **21**, 861 (1980).
[18] R. Machleidt, K. Holinde, and Ch. Elster, Phys. Rep. **149**, 1 (1987).
[19] R.W. Wiringa, R. Smith, and T.L. Ainsworth, Phys. Rev. C **29**, 1207 (1984).
[20] P. Wilhelm, W. Leidemann, and H. Arenhövel, Few-Body Syst. **3**, 111 (1988).
[21] H.J. Weber and H. Arenhövel, Phys. Rep. **36**, 279 (1978).
[22] W. Leidemann and H. Arenhövel, Nucl. Phys. **A465**, 573 (1987).
[23] S. Galster, H. Klein, J. Moritz, K.H. Schmidt, D. Wegener, and J. Bleckwenn, Nucl. Phys. **B32**, 221 (1971).
[24] W. Leidemann, K.-M. Schmitt, and H. Arenhövel, Phys. Rev. C **42**, R826 (1990).

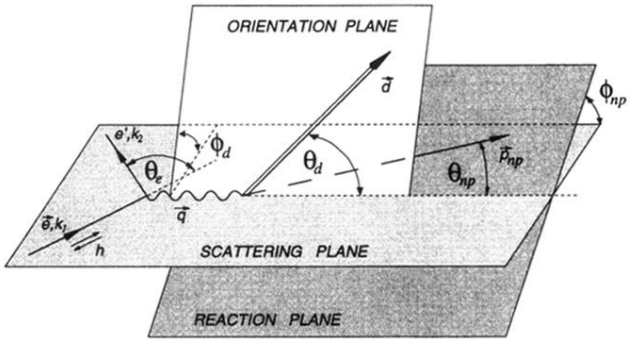

FIG. 1. Geometry of exclusive electron-deuteron scattering with polarized electrons and an oriented deuteron target. The relative n-p momentum defining with $\vec{q}$ the reaction plane is denoted by $\vec{p}_{np}$ and is characterized by angles $\theta = \theta_{np}$ and $\phi = \phi_{np}$. The deuteron orientation axis forming with $\vec{q}$ the orientation plane is denoted by $\vec{d}$ and specified by angles θ_d and ϕ_d.